EUROPEAN ORGANIZATION FOR NUCLEAR RESEARCH

CERN-EP/82-195
December 3rd, 1982

SOFT π^-p AND pp ELASTIC SCATTERING IN THE ENERGY RANGE 30 TO 345 GeV

J.P. Burq[*], M. Chemarin[*], M. Chevallier[*], A.S. Denisov[**], C. Doré[***], T. Ekelöf[++,+], J. Fay[*], P. Grafström[++,+], L. Gustafsson[+], E. Hagberg[+], B. Ille[*], A.P. Kashchuk[**], G.A. Korolev[**], A.V. Kulikov[**], S. Kullander[+], M. Lambert[*], J.P. Martin[++,*], S. Maury[++,***], M. Querrou[***], V.A. Schegelsky[**], E.M. Spiridenkov[**], I.I. Tkach[**], M. Verbeken[***] and A.A. Vorobyov[**]

Submitted to Nuclear Physics B

---

* Institut de Physique Nucléaire, IN2P3, Université de Lyon-Villeurbanne, France.

** Leningrad Nuclear Physics Institute, Gatchina, USSR.

*** Laboratoire de Physique Corpusculaire, IN2P3, Université de Clermont-Ferrand, Aubière, France.

\+ The Gustaf Werner Institute, University of Uppsala, Sweden.

++ At present, CERN, Geneva, Switzerland.

0021P/bg

ABSTRACT

Differential cross-sections for $\pi^- p$ and pp elastic scattering have been measured at incident momenta ranging from 30 to 345 GeV and in the t-range $0.002\ (GeV/c)^2 \leq |t| \leq 0.04\ (GeV/c)^2$. From the analysis of the data, the ratio $\rho\ (t=0)$ of the real to the imaginary parts of the forward scattering amplitude was determined together with the logarithmic slope b of the diffraction cone.

The results on the real parts confirm the validity of the forward dispersion relations at high energies. Using the dispersion relations, it was shown that the experimental data on $\rho_{\pi^- p}(t=0)$ require a continuous rise of the total πp cross-sections at least up to the energy of 2000 GeV revealing thus a close similarity in high energy behaviour of πp and pp interactions.

The results on the slope parameters from this experiment together with the analysis of the available world data demonstrate that the existing experimental data are consistent with the hypothesis of a universal shrinkage of the hadronic diffraction cone at high energies. The value of the asymptotic shrinkage parameter α'_P was found to be independent on the kind of the incident hadron and on the momentum transfer in the t-range $|t| \leq 0.2\ (GeV/c)^2$: $2\alpha'_P = (0.28 \pm 0.03)(GeV/c)^{-2}$.

1. INTRODUCTION

Measurements of soft elastic scattering of hadrons can be used to obtain the real part of the forward hadronic amplitude by analysis of the interference between the hadronic and the Coulomb amplitudes. Dispersion relations relate the real part to the total hadronic cross-section. These relations are such that the real part at a given energy is sensitive to the behaviour of the total cross-section at energies above that energy. This possibility of using this method to probe the behaviour of the πp interaction at high energies, where direct measurements of the total cross-section are not available, has been the primary motivation for the present investigation.

The theoretical derivation of the dispersion relations is based on the general assumptions of unitarity, crossing symmetry and analyticity of the scattering amplitude. Furthermore, the condition of analyticity is related to the validity of causality at small space-time distances. A strict derivation of the dispersion relations has been made in the case of πp scattering [1]. Therefore, the experimental verification of the πp dispersion relations at the highest possible energies represents a case of particular interest. The verification can be made by comparing the value of the real part calculated on the basis of the dispersion relations with that found in the Coulomb interference experiments in an energy region well below the maximum energy up to which experimental data of the total cross-sections are available. For such energies, the real part can be calculated without the ambiguity related to the lack of knowledge of the asymptotic behaviour of the total cross-sections.

Another parameter that can be studied in small angle elastic scattering experiments is the logarithmic slope b of the differential cross-section. In the optical model this parameter is directly related to the geometrical size of the interacting hadrons. According to the classical Pomeron theory [2] the slope should increase logarithmically at energies sufficiently high for Pomeron exchange to dominate as $b(s) \propto 2\,\alpha_P' \ln s$, where the shrinkage parameter α_P' should have the same value for all hadrons. Furthermore, α_P' should have no strong t-dependence at small values of t. Until now this theorem of universal shrinkage of the elastic cone did not seem to be satisfied by the available high energy data. In particular, the logarithmic increase of b(s) was believed to have been

established in pp-scattering at $s > 100$ GeV^2 in the t-range $0.02 \lesssim |t| \lesssim 0.12$ (GeV/c)^2. In this case, the shrinkage parameter was reported [3,4] to be $\alpha'_{pp}(-t = 0.07 \text{ (GeV/c)}^2) = 0.278 \pm 0.024 \text{ (GeV/c)}^{-2}$. However, at bigger t-values, considerably smaller values of α'_{pp} were found: [4] $\alpha'_{pp}(-t = 0.2 \text{ (GeV/c)}^2) = 0.100 \pm 0.062 \text{ GeV/c)}^{-2}$. Also, the shrinkage parameter for $\pi^{\mp}$ p diffraction appeared to be small at $-t = 0.2$ (GeV/c)^2 where most of the experimental data had been obtained. At smaller t-values the data on $\pi^{\mp}$ p scattering were scarce, and it was not possible to evaluate the s-dependence of the slope parameter there.

With the aim to investigate the questions discussed above we have measured the absolute differential cross section for elastic scattering in the t-range $0.002 \lesssim |t| \lesssim 0.04$ (GeV/c)^2 at energies ranging from 30 GeV to 345 GeV for π^-p scattering and from 100 GeV to 300 GeV for pp-scattering. From the measured cross-sections, the ratio of real to imaginary part ρ of the forward scattering amplitude and the slope parameter b at $\langle -t \rangle = 0.02$ (GeV/c)^2 have been determined.

The method used for these measurements is based on simultaneous observation of the forward-scattering beam particle and of the recoiling target particle which allows kinematical constraints to be used for the elimination of background. With these constraints the separation of the elastic events from the background could be made to a satisfactory degree also at the highest energies in the experiment. Two other features of our experimental method are the high t-resolution in the Coulomb interference region ($\sigma(t) \simeq 10^{-4}$ (GeV/c)^2) and the absolute normalization of the differential cross-sections of a precision ± 1%.

The experimental programme was carried out at the CERN Super Proton Synchrotron (SPS). The first measurements were made in the H3 beam in the West Area (WA9-experiment) at energies between 30 and 140 GeV and further measurements in the H8 beam in the North Area (NA8-experiment) at energies between 100 and 345 GeV. Short descriptions of both set-ups have already been published together with brief accounts of the results [5-10]. In the present paper we give a more detailed description of the NA8-experiment. The discussion of the data in the last section of this paper is based on the results of both the WA9 and the NA8 experiments.

2. EXPERIMENTAL SET-UP

In fig. 1, a schematic lay-out of the NA8 experiment is given, showing the beam spectrometer, the particle identifiers, the forward spectrometer, the recoil detector IKAR, and the trigger scintillators. Some features of the lay-out have already been described in an earlier publication [8] together with the results from the πHe and pHe elastic scattering measurements which were performed using the same set-up. Below, only a brief description of the various parts of the lay-out is given, and the reader is referred to ref. [8] for more details.

The secondary beam was derived from a 400 GeV primary proton beam. The beam was focused onto the recoil detector IKAR. The dimensions of the beam spot at focus were about 10x10 mm^2, and the beam divergency was about 0.2 mrad. A high-resolution beam spectrometer, provided as a general facility in the H8 beam [11], gave information on the momentum p of each beam particle within the momentum bite defined by the momentum slit. The resolution of the beam spectrometer was $\sigma(p)/p = 0.05\%$. The momentum defining collimator was used also to maintain the intensity of the secondary beam at a level of 10^6 particles per 1 s effective spill length by varying the collimator acceptance between $\Delta p/p = .8\%$ and .2%. The intensity of the primary beam required by the experiment was about $3 \cdot 10^{11}$ protons per burst at beam momenta up to 300 GeV/c and 10^{12} protons per burst at the higher beam momenta. The burst cycle was 10.8 s. The mean absolute momentum of the beam particles p* was determined in the helium experiment [8] with a precision of 0.15%. The results of this calibration of the beam momentum are presented in table 1, and the details of the procedure can be found in a separate paper [6]. The measured values of p* were found to be very close to the nominal values of the beam momentum p_o determined from magnetic field measurements of the bending magnets in the beam line.

The incident particles were identified using two helium filled differential Cerenkov counters [12] (CEDAR1 and CEDAR2) and two threshold counters (TH1 and TH2). As an example fig. 2 shows a particle spectrum at 150 GeV/c obtained by scanning the pressure in one of the CEDARs. The figure shows clear separation between pions, kaons, and antiprotons. Similar scans were made at all momenta, and the beam composition as determined at the position of the CEDARs is given in table 1. In the

experiment, different combinations of the Cerenkov counters have been used at different energies to distinguish the particles. For example, at 150 GeV/c CEDAR1 was tuned on K, CEDAR2 on p, and both threshold counters were set to count π and K. The information from all four counters was read out for each event, and the particles were labelled according to the following combinations:

$$\pi = (TH1 \cup TH2) \cdot \overline{CED1} \cdot \overline{CED2}$$
$$p = \overline{(TH1 \cup TH2)} \cdot \overline{CED1} \cdot CED2$$
$$K = (TH1 \cup TH2) \cdot CED1 \cdot \overline{CED2}$$

This method thus provided a complete particle separation, and it was therefore possible to collect statistics for all kinds of particles simultaneously. With increasing beam momentum the efficiency of the Cerenkov counters dropped from $\sim$ 95% at 100 GeV/c down to $\sim$ 50% at 300 GeV/c. This did not present a problem for the identification of the dominating particles (π^- and p) in the beam. At 325 GeV/c and 345 GeV/c no identification was needed as the beam contained practically only pions.

The Cerenkov counters could not be used to distinguish electrons and muons from pions. The muons were identified and eliminated with two scintillator counters interspaced by 1 meter of iron. These counters were placed downstream of the beam stopper. For the rejection of the electrons, an electromagnetic shower detector was used, consisting of 18 scintillator counters interspaced by lead plates and iron blocks. The transverse dimensions of the e and μ counters were large enough to provide 100% geometrical acceptance throughout the t-range covered by the measurements. As the counters were placed in the downstream end of the set-up, events corresponding to the hadrons that decayed in the space covered by the set-up were also rejected. The percentages of the beam particles rejected using the μ and e counters are shown in table 1. These values may be considered as upper limits for the contaminations of the electrons and muons in the beam.

The recoil detector IKAR [13,14] is an ionization chamber filled with pure hydrogen at 10 atm pressure. IKAR consists of six identical cells, two of which are shown in fig. 3. Each cell contains an anode plate, a cathode plate, and a wire grid. The anode plate is divided into three rings

(A,B, and C). The anode A is 194 mm in diameter, and the external and internal diameters of the anode B are 206 mm and 390 mm respectively, and those of the anode C, 410 mm and 480 mm. The distance d between the cathode and the grid is 100.0 ± 0.1 mm. The precise value of d was important for the determination of the effective target thickness.

After an elastic collision the recoiling proton will ionize the gas along its path. A signal will be induced on the cathode immediately after the collision when the electrons start to drift towards the anode plate. The anode signals will appear only when the electrons drift through the grid. The electron drift time from the cathode to the grid was 21 μs. The following informations were recorded for each event. Fast timing signals S_K, S_A, and S_B were obtained from the cathode shapers, anode A shapers, and anode B shapers, respectively (fig.4), and the delay times t_K, t_A, and t_B of these signals with respect to the passage of the beam particle were recorded. The amplitudes V_A, V_B, and V_C of the anode pulses were also measured and recorded as well as the amplitude V_{AB} of the analog sum of the signals from the anodes A and B. The rise-time of the V_{AB} pulse was also recorded and used to determine the length of the recoil track projection X_r on the beam axis. The longitudinal position of the recoil track was found from the delay time t_A: $z_r = t_A \cdot W$, where z_r is the distance from the grid to the nearest end of the recoil track within the anode A zone, and W is the electron drift velocity.

The amplitudes V_A, V_B, V_C, and V_{AB} are proportional to the energies T_A, T_B, T_C, and T_{AB} left by a recoil in the corresponding parts of the sensitive volume of IKAR. As a first approximation, the calibration of the energy scale was made with the aid of α-sources deposited on each cathode, and the recoil energies were determined according to the formula:

$$T_i = V_i \cdot \frac{E_\alpha}{V_{\alpha i}} \, (1 - \delta_a(z_r)), \qquad i = A,B,C,AB. \tag{1}$$

where

$E_\alpha = (E_\alpha^{(o)} - \Delta_{abs})$ is the α-particle energy corrected for the energy absorption in the α-source, $E_\alpha^{(o)} = 4.777$ MeV [15], $\Delta_{abs} = 10 \pm 5$ keV;

$V_{\alpha i}$ is the mean amplitude of the pulses on the i-th anode produced by the α-particles;

V_i is the amplitude of a pulse on the i-th anode produced by a recoiled proton;

$\delta_a(z_r)$ is a correction which takes into account the limited transparency of the grid and the loss of the drifting electrons through adhesion to electronegative impurities in the gas.

These losses were continously controlled by measuring the difference ΔG_α in the positions of two α peaks corresponding to α-particles emitted from the sources deposited on the grid and on the cathode, respectively. The correction was calculated as

$$\delta_a(z_r) = \frac{(d - z_r)}{d} \cdot \frac{\Delta G_\alpha}{V_{\alpha i}} . \qquad (2)$$

where d is the cathode-grid distance.

The value of $\Delta G_\alpha / V_{\alpha i}$ was about 1% after refilling IKAR with fresh hydrogen, then increasing by 0.05% per day. Note, that we used commercial hydrogen of the highest purity grade (Hydrogen N60 supplied by Carbogas SA).

If the recoil proton stops inside IKAR then the measured ionization energy T_{AB} is equal to the recoil kinetic energy T_r. Otherwise the energy deposited in IKAR can be used to derive T_r using the relation between energy and range of protons in hydrogen gas at 10 atm pressure (fig. 5).

The energy and the time resolution of IKAR was determined essentially by the fluctuations of the ionization produced by the beam particles which traverse the sensitive volume of IKAR. Each beam particle leaves about 40 keV in each IKAR cell. The corresponding signals on the chamber electrodes were suppressed by sending pulses of the same amplitude, but opposite polarity, to the electrodes each time a beam particle passes through the chamber. This procedure helped to avoid a systematic shift in the measured recoil energy and also improved the energy resolution of IKAR. However, it could not exclude the fluctuations due to production of δ-electrons by the beam particles. At the beam intensity of 10^6 particles per 1 s spill the standard error due to these fluctuations was $\sigma(T_{AB}) = 70$ keV. The corresponding resolution in the four-momentum transfer squared was $\sigma(t) = 1.3 \cdot 10^{-4} (\mathrm{GeV/c})^2$ in the t-range $0.002 < |t| < 0.008\ (\mathrm{GeV/c})^2$. Table 2 summarizes the parameters of the recoiled and scattered particles measured with IKAR and with the forward spectrometer and the precision of the measurements obtained under actual running conditions.

The forward spectrometer served to determine the scattering angle Θ and the momentum p' of the forward scattered particles. The spectrometer included four bending magnets B5-B8 and six blocks of multiwire proportional chambers PC1-PC6. Each block contained two or more planes of MWPCs to measure six horizontal (x_1 to x_6) and four vertical (y_1 to y_4) coordinates of the forward particle trajectory. More details about the forward spectrometer and about the mode of operation of the MWPCs can be found in refs. [8,16]. The space resolution in the MWPC blocks was $\sigma(x_{1-5}) \simeq \sigma(y_{1-4}) \simeq 0.15$ mm and $\sigma(x_6) \simeq 0.3$ mm. The angular resolution shown in table 2 includes also the Coulomb scattering effect. Tracing the trajectories of the beam particles into IKAR, it was possible to determine the x_r and y_r coordinates of the vertex with a precision of $\pm$ 0.15 mm. The current in the forward spectrometer magnet was adjusted to give a deflection angle of 15 mrad at all energies, and the momentum resolution varied from 0.2% to 0.3%. The detection efficiency of each MWPC block was close to 100%. The exact value of this efficiency was permanently measured using beam particles as explained in section 4.

The scintillator counters S1A, S1B, S2A, S2B, A1, A2, A3 were used to trigger the system. The dimensions of the counters are given in ref. [8]. Special care was taken to provide a negligible inefficiency of the counter S2 $\equiv$ S2A U S2B. The global and the local efficiencies of this counter were under permanent control. An important source of background in IKAR were showers produced by the beam particles in the material in the beam line upstream of IKAR. An effective elimination of the shower background was achieved with the shower detector A3 placed just downstream of IKAR. This counter produced a signal when at least three particles were registered outside the central opening of 50x50 mm^2. To avoid the possible suppression of elastic events accompanied by bremstrahlung gammas, veto counters were excluded downstream of IKAR.

3. MONITOR, TRIGGER AND DATA TAKING.

The first-level trigger was given by a coincidence

$$TR1 = S1A \cdot S1B \cdot (S2A \cup S2B) \cdot \bar{A}_1 \cdot \bar{A}_2 \cdot \bar{A}_3 .$$

It was required that within $\pm$80 ns with respect to the trigger there was no other beam particle. This trigger strobed the MWPCs in blocks PC1-PC4 and gave a start to a Special Digital Processor Unit (SDPU) [17].

The SDPU received information from PC1, PC2, and PC4. A flag P_{in} was set by the SDPU in case it was possible to reconstruct the incoming particle trajectory in blocks PC1 and PC2, and a flag P_{out} was set if the track was reconstructable in block PC4. This allowed to form logically the monitor signal

$$MON = P_{in} \cdot P_{out} \cdot TR1.$$

These signals, counted by a scaler, were used to normalize the measured cross-sections. In the case of MON=1 the SDPU calculated the projected scattering angles θ_x and θ_y. If any of these projections was bigger than or equal to a preset value θ_o, a second-level trigger was produced by the SDPU:

$$TR2 = MON \cdot [(\theta_x > \theta_o) \cup (\theta_y > \theta_o)].$$

The events with MON=0 or TR2=0 were rejected. Thus the SDPU acted as a beam killer. With a threshold value θ_o corresponding to $|t| = 0.7 \cdot 10^{-3}$ $(GeV/c)^2$ the reduction in the trigger rate was about 100. The dead time introduced by the SDPU was 250 ns.

The second-level trigger strobed the MWPCs in blocks PC5, PC6, BS1-BS4 and opened a 4 μs gate for the IKAR cathode shapers and a 25 μs gate for the anode shapers. The second-level trigger also gave a start signal to a second processor (REPS; Ring Evaluation Processor System) which calculated the scattering angle using the projected values (θ_x, θ_y) given by the SDPU: $\theta^2 = \theta_x^2 + \theta_y^2$. The REPS compared this value with the preset angles θ_1 and θ_2 that corresponded to the recoil energy of respectively 300 keV and 30 MeV and provided a rejection signal:

$$REJ = TR2 \cdot \left[(\theta^2 < \theta_1^2) \cup (\theta^2 > \theta_2^2)\right].$$

This allowed to select events in a defined recoil energy range. The REPS gave its decision in 2.25 μs and reduced the trigger rate by a factor of 2. The probability for a good event to be rejected by the SDPU and by the REPS was estimated with a Monte Carlo simulation which took into account the experimental angular resolution of the forward spectrometer, and it was found that the number of rejected events in the used t-range was negligible.

A special signal (RC-signal) was produced by the REPS if $\theta^2 > \theta_3^2$ where θ_3 is the angle corresponding to a recoil energy of 5 MeV, which is the energy value above which the whole recoil track is not contained within the ionization chamber:

$$RC = TR2 \cdot (\theta^2 > \theta_3^2).$$

The RC-signal helped to avoid the problem of cathode inefficiency at large t-values as explained below. Normally, the data acquisition system was triggered, if a cathode signal S_K arrived within 4 μs, followed by an anode signal $S_A \cup S_B$ within 25 μs. However, for the highest scattering angles, the energy deposited in IKAR by the recoiling proton decreased down to 1 MeV, and the inefficiency of the cathode shapers became important. To avoid this problem, the cathode shapers were excluded from the trigger condition each time the RC-signal appeared. The price for this was some decrease in the rejection factor provided by IKAR. However, the decrease in the rejection was small due to the fact that the rate of the RC-signals was an order of magnitude less than that of the SDPU triggers.

A digital discriminator was included in the read out system, which compared the amplitudes V_A and V_{AB} with the preset thresholds 120 keV and 310 keV respectively. Only those events which had V_A and V_{AB} values greater than the thresholds were acquired by the computer. The rejection factor due to IKAR and the digital discriminator was about 60. Finally, as a result, about 80 events were written on magnetic tape for each burst. Each event contained about 250 words of 16 bits.

Some of the events were disturbed by the particle showers that were created in the beam line upstream of IKAR and which traversed IKAR during its registration time. Such events were suppressed in the off-line analysis using a "shower" flag which was set when a coincidence between the A_3 counter signals and the cathode shapers signals was detected during a 30 μs interval after the first-level trigger.

4. DATA ANALYSIS

The data analysis was performed in two stages. In the first stage, data summary tapes (DST's) were produced. The events to be written on the DST's were selected using the sequence of criteria listed below.

i) Muons events were eliminated by requiring that at least one of the two muon counters produced a signal that exceeded threshold. This algorithm provided close to 100% efficiency for rejection of muons with only a small loss of hadrons (0.4%).

ii) The electromagnetic shower detector was used to eliminate electron events. This was made on the basis of the sum of the signals from scintillators and the longitudinal size of the shower.

iii) It was required that the forward particle track should be reconstructable in each PC block separately.

iv) Only incoming particles with trajectories providing full geometrical acceptance in the detectors downstream of IKAR were accepted.

v) The momentum of the scattered particle should be within ±5% of the momentum of the incident beam particle.

vi) There should be only one IKAR cell with V_A and V_{AB} amplitudes higher than the levels of the digital discriminator.

vii) There should be no showers detected by the A_3 counters in coincidence with cathode pulses during the registration time of IKAR.

It was checked that the rejection power of these criteria was independent on the momentum transfer.

Also, a cut in z_r values was applied to exclude the regions near the grid and near the cathode:

$$z_{min} < z_r < z_{max},$$

where z_{min} = 20 mm and z_{max} = 80 mm.

This cut was needed to eliminate the elastic events for which the end of the recoil track could reach the electrodes. (Note that $X_r \simeq 20$ mm at $|t| = 0.04$ $(GeV/c)^2$). It also reduced the background induced by reactions in material of the electrodes.

To illustrate the quality of the data at this stage, fig. 6 shows the correlation between the ionization energy deposited by the recoil in IKAR and the kinetic energy of the recoil as derived from the forward scattering angle. In this figure one can clearly distinguish the elastic events above the background. The reason for the drastic increase of the background at $T_r > 5$ MeV is that no coincidence with the IKAR cathode signals was required in this T_r-region as already described. However, these accidentals could be eliminated in the analysis as discussed below.

To control the losses of good elastic events due to the different selection criteria, so called test events were used. These were events where recoil signals were simulated by a test generator sending electronic signals of variable amplitudes to each cell of IKAR. The signals were sent in coincidence with a beam particle, and the whole apparatus was read out for each test event. Typically 10 test events were registred each burst. By applying the criteria listed above to the test events the global inefficiency for the detection of good elastic event could be determined.

Table 3 gives an example of the percentage of test events eliminated by each criteria. The typical global inefficiency was $\varepsilon_g \simeq 13\%$. The statistical error in the measurement of this value was negligeable as the total number of test events collected was always larger than 10^5 for each beam energy.

In the second stage of the analysis the elastic events on the DST were further selected using the different kinematical correlations between the measured parameters. For this purpose the events were divided into two classes. The first class was characterized by the recoil proton being stopped inside the active volume of the recoil detector. The second class thus contained the events for which the recoil track escaped outside the recoil detector.

For the first class the following two correlations were used:

$$\Delta T_r = T_r^* - T_r = F_1 (T_r^*), \tag{3}$$

$$X_r = F_2 (T_r^*). \tag{4}$$

Here, X_r is the recoil track projection on the beam axis,

T_r is the recoil energy calculated from V_{AB} amplitude according to eq.(1),

T_r^* is the recoil energy calculated from the scattering angle of the forward particle assuming elastic scattering:

$$T_r^* = (p^*\theta)^2/2M_p, \tag{5}$$

where p^* is the mean absolute momentum of the beam particles and M_p is the proton mass.

The scattering angle was calculated according to

$$\theta^2 = \theta_x^2 + \theta_y^2 - 2\,\sigma_{\theta\,\mathrm{proj}}^2 . \tag{6}$$

θ_x and θ_y were found from the parameters of a straight line fit of the particle trajectories upstream and downstream of IKAR, and $\sigma_{\theta\mathrm{proj}}$ is the forward scattering angular resolution.

For the second class of events three correlations were used

$$X_r = F_2 (T_r^*), \tag{7}$$

$$\Delta R_A = R_A^* - R_A = F_3 (T_r^*). \tag{8}$$

$$\Delta R_B = R_B^* - R_B = F_4 (T_r^*), \tag{9}$$

where R_A^* and R_B^* are the calculated projections of the recoil track to the A and B anode planes, respectively.

These projections were calculated using the vertex position and the azimuthal scattering angle. R_A and R_B are the same quantities but determined from the V_A and V_B pulse heights of IKAR using the α-source calibration and the energy-range relation.

Using the above defined functions a χ^2-distribution was defined for each class:

$$\chi_1^2 = \left(\frac{\Delta T_r - F_1(T_r^*)}{\sigma_1(T_r^*)}\right)^2 + \left(\frac{X_r - F_2(T_r^*)}{\sigma_2(T_r^*)}\right)^2 \tag{10}$$

$$\chi_2^2 = \left(\frac{\Delta R_A - F_3(T_r^*)}{\sigma_3(T_r^*)}\right)^2 + \left(\frac{\Delta R_B - F_4(T_r^*)}{\sigma_4(T_r^*)}\right)^2 + \left(\frac{X_r - F_2(T_r^*)}{\sigma_2(T_r^*)}\right)^2 \tag{11}$$

The functions $F_i(T_r^*)$ as well as the standard deviations $\sigma_i(T_r^*)$ were determined in an iterative procedure using the experimental data.

An elastic event was then defined as an event having $\chi^2 < \chi^2_{cut}$ where $\chi^2_{cut} = 15$ and $\chi^2_{cut} = 20$ for the two classes respectively. Figs. 7 to 10 display some distributions of the elastic events left after the χ^2-cut. Note, that the distributions shown in figs. 8, 9, and 10 were not used to form the χ^2-distributions (10) and (11). These figures thus demonstrate the level of the remaining background which is due to accidentals and inelastic scattering. As can be seen in figure 10, the low momentum tail of the p'-distribution is very small. Moreover, the magnitude and the t-dependence of the tail agree with the assumption that most of the tail is due to bremsstrahlung of the scattered pions. A comparison between the π^-p, pp, and π^-He, pHe [8] data supports this assumption.

To produce the differential cross-sections dσ/dt we need an absolute calibration of the t-scale. The t-value was determined differently for the two classes of events. For the second class of events t was calculated from the forward scattering angle as

$$-t = (p^*\theta)^2. \tag{12}$$

The $(p^*\theta)^2$-scale was calibrated with a precision of 0.1% in a special experiment [6]. For the events with the recoil stopped in IKAR, the recoil energy measurement was used to determine t because of the better t-resolution provided by IKAR. The α-source calibration was corrected with the experimentally found function $F_1\ (T_r^*)$ according to

$$-t = 2M_p \cdot (T_r + F_1\ (T_r^*)). \tag{13}$$

$F_1\ (T_r^*)$ is illustrated in fig. 11. A straight line fit

$$F_1\ (T_r^*) = a_o + a_1 T_r^* \tag{14}$$

describes the data well in the energy interval 1 MeV $\leq T_r^* \leq$ 5 MeV with $a_o = (-45 \pm 5)$ keV and $a_1 = 0.020 \pm 0.002$.

From these considerations we conclude that the t-scale is calibrated in the t-range covered by the experiment with a precision better than 0.5%.

The fact that $F_1\ (T_r^*) \neq 0$ is due to differences in the primary ionization and in recombination of the ions produced by α-particles and by protons of the same energy. Varying the pressure in IKAR we have measured the recombination to be 1.8% for α-particles of 5 MeV. Taking this into account, and assuming recombination to be small for protons, we conclude that 5 MeV α-particles produce about 3% more ions in hydrogen than protons of the same energy.

The differential cross-section was calculated using the formula:

$$\frac{d\sigma}{dt} = \frac{N}{\Delta t} \cdot \frac{1}{I} \cdot \frac{1}{N_p} \cdot \frac{1}{(1-\varepsilon_g)} \tag{15}$$

where Δt is the width of the t-bin,

N is the number of events in the t-bin,

ε_g is the global inefficiency,

I is the total number of incident beam particles as registered by the SDPU monitor,

and N_p is the number of protons per 1 cm² in the target:

$$N_p = n \cdot L$$

where n is the proton density in cm^{-3} and L is the length of the gas target in cm.

The value of n was determined from the measured gas pressure and temperature through the Van-der-Vaals equation with an estimated precision of 0.1%. By definition $L = z_{max} - z_{min} = W\,[(t_A)_{max} - (t_A)_{min})]$. The absolue value of drift velocity W was measured in a special run where the cathode signal was not required in the trigger thus providing an efficient detection of events near the grid. Fig. 12 shows the t_A-distribution of the events accumulated in this run. Experimental points were fitted to a formula including a gaussian centered around the observed peak and taking into account the t_A resolution and background. From the fit, the grid position $(t_A)_G$ and the cathode position $(t_A)_K$ were determined with a precision better than 50 ns. Then W was calculated as

$$W = d \;/\; [(t_A)_K - (t_A)_G] \tag{16}$$

and the value of L as

$$L = d\,\frac{(t_A)_{max} - (t_A)_{min}}{(t_A)_K - (t_A)_G}\quad . \tag{17}$$

Here, d is the cathode-grid distance, d = (100.0 ± 0.1) mm. The delay times were measured using a quartz pulse generator (20 MHz). As a result, the absolute value of L could be determined with a precision of 0.4%. It should also be noted that the determination of L is independent of the value of t.

To get the final differential cross section the following corrections were applied.

1. Some good elastic events were eliminated by the χ^2-cut. To estimate the number of such events the above mentioned test events were used to simulate the experimental χ^2-distribution. By applying the same cut to the χ^2-distribution of the test events the losses have been determined (fig. 13).

2. The χ^2-distribution formed by the test events was also used to estimate the level of background events with $\chi^2 < \chi^2_{cut}$. Properly normalized it was subtracted from the χ^2-distribution of the physical events and the remaining events were considered as the background. Fig. 13 illustrates this procedure.

3. At small t-values the inefficiency of the cathode shapers was important. However, it was possible to determine this inefficiency experimentally with high precision using the second class of events with the energy deposited in the cathode zone of IKAR ranging from 0.8 MeV to 2 MeV. For such events no cathode signal was required in the trigger, and the cathode inefficiency could be determined from relative fraction of events which did not have the cathode shaper flag.

4. A correction was introduced to take into account the rejection due to the momentum cut of good elastic events accompanied by bremsstrahlung. The formula employed for this correction were derived from a general expression given in ref. [18]

$$(d\sigma/dt)^{corr} = (d\sigma/dt)^{meas} \quad [1 + \delta_r(t)] \tag{18}$$

where $(d\sigma/dt)^{corr}$ and $(d\sigma/dt)^{meas}$ are the corrected and the measured cross-sections, respectively, and

$$\delta_r(t) = \frac{2\alpha}{\pi} \cdot \ln(p/\Delta p) \quad \left[\frac{(2m^2 - t)}{Q} \cdot \ln \frac{Q - t}{Q + t} - 1 \right] \tag{19}$$

where

$Q = (t^2 - 4t \cdot m^2)^{0.5}$;

α = the fine structure constant;

m = the projectile mass;

Δp = the maximum loss accepted by the momentum cut.

In our case $\Delta p/p = 0.05$, and the bremsstrahlung correction for πp scattering was $\delta_r = 0.07\%$ at $-t = 0.002$ (GeV/c)^2 and $\delta_r = 0.7\%$ at $-t = 0.04$ (GeV/c)^2.

Fig. 14 shows all the above mentioned corrections as function of recoil energy. The possible uncertainties in these corrections are estimated to produce a systematical error in $d\sigma/dt$ determination of not more than 0.4%. The other systematical errors are enumerated in table 4.

The corrected differential cross-sections for pion-proton and proton-proton scattering are given in table 5. The total error in normalization of these cross-sections is estimated to be ±1%.

5. RESULTS OF THE FITS TO THE EXPERIMENTAL DATA

The differential cross-sections have been fitted with the following parametrization:

$$\frac{d\sigma}{dt} = K \left\{ \frac{4\pi\alpha^2\hbar^2}{\beta^2|t|^2} \cdot G_h^2 G_p^2 + (1+\rho^2) \cdot \frac{\sigma_{hp}^2}{16\pi\hbar^2} \cdot e^{-b|t|} + \frac{\sigma_{hp}\alpha}{\beta|t|}(-\sin\delta - z_h \cdot \rho\cos\delta) \cdot e^{-b|t|/2} \cdot G_h G_p \right\}, \text{ mb/(GeV/c)}^2 \quad (20)$$

where K is the normalization parameter,

α is the fine structure constant (1/137),

β is the velocity of the incident particle,

σ_{hp} is the total hadronic cross-section on proton (mb),

ρ is the ratio of the real to imaginary parts of the forward elastic scattering amplitude,

b is the logarithmic slope of the differential hadronic elastic cross-section ((GeV/c)$^{-2}$),

G_h is the electromagnetic form factor of the incident hadron [19] $G_\pi = (1 + |t|/0.59)^{-1}$ and $G_p = (1 + |t|/0.71)^{-2}$,

z_h is the sign of the charge of the incident hadron,

$\delta = -[\ln(|t|/0.092) + 0.577] \cdot \alpha/\beta$ is the Coulomb phase [20]

$\hbar = 0.624$ GeV $\cdot \sqrt{\text{mb}}$.

The normalization parameter K was constrained to be equal to unity within ±1%. Data from the total cross-section measurements of Carroll et al. [21] were used to constrain the values of σ_{hp}. Note, that in eq. (20) the spin effects have been neglected.

Two fits to the data were made. In the first fit both ρ and b were left as free parameters and the fit was made using the data in the full t-range at each energy. In the second fit, only data in the lower t-region ($|t| < 0.009$ $(GeV/c)^2$), in which the momentum transfer was determined from the recoil measurement, was used. Furthermore, in the latter fit, only ρ was left as a free parameter and b was fixed to the value obtained in the first fit.

Two examples of such fits are given in fig. 15a and fig. 15b. As seen from the figures, the difference between the results of the two different kind of fit is not significant. The results from the first fit are presented in table 6. The errors given include statistical errors, the quoted error in the normalization parameter and the errors in σ_{hp} as given in ref. [21]. A shift in the value of σ_{hp} of +0.1 mb would shift the ρ-values by -0.004 in the case of π^-p scattering and by +0.004 in the case of pp scattering. The sensitivity to the b-values in the fits where b is fixed is very small: $d\rho/db = +0.003$ $(GeV/c)^2$ for π^-p scattering and $d\rho/db = -0.003$ $(GeV/c)^2$ for pp scattering.

Table 6 presents also the results of the WA9 experiment performed in the energy range 30 to 140 GeV. Note, that our previously published results [5,7] on the slope parameters have been corrected by $\Delta b = -0.5$ $(GeV/c)^{-2}$. This change is due to the introduction of the correction for bremsstrahlung and of an efficiency correction at big t-values which were neglected in the previous analysis. However, these corrections did not produce any change in the values of ρ.

6. DISCUSSION

6.1 Validity of the forward dispersion relations at high energies.

The real part of the forward elastic scattering amplitude is related to the total cross-sections through the forward dispersion relations (FDR). At high energies the once subracted FDR can be presented in a simplified form:

$$\rho_{h^{\pm}p}(E,t=0) = I^{+}(E) \mp I^{-}(E) + \frac{C_o}{E \cdot \sigma_{h^{\pm}p}(E)} \quad , \tag{21}$$

$$I^{+}(E) = \frac{2E}{\pi \sigma_{h^{\pm}p}(E)} \oint_{m_h}^{\infty} \frac{\sigma_{hp}^{+}(E')}{(E')^2 - E^2} dE' \quad , \tag{22}$$

$$I^{-}(E) = \frac{2}{\pi \sigma_{h^{\pm}p}(E)} \oint_{m_h}^{\infty} \frac{\sigma_{hp}^{-}(E')}{(E')^2 - E^2} E' dE' \quad , \tag{23}$$

where $E = \sqrt{m_h^2 + p^2}$ is the total laboratory energy of the incident particle; m_h is the mass of the incident particle;

$$\sigma_{hp}^{+} = \frac{\sigma_{h^-p} + \sigma_{h^+p}}{2} \quad , \quad \sigma_{hp}^{-} = \frac{\sigma_{h^-p} - \sigma_{h^+p}}{2} \quad ,$$

and $\sigma_{h^{\pm}p}$ are the total cross-sections.
The parameter C_o is a constant of subtraction to be determined from low energy data on $\rho_{hp}(t=0)$.

The experimental test of the FDR is of particular interest in the case of πp-scattering as compared to pp scattering for the following reasons:

i) in the case of πp-scattering there exists a strict derivation of the FDR from fundamental principles;

ii) the constant C_o can be calculated with a satisfactory precision from low energy πp-data. The value of C_o is in fact so small that the last term in (21) is negligible [22] for $E > 10$ GeV;

iii) the interference formula (20) is better justified as there is no spin effects in small angle πp scattering;

iv) the precision of calculation of the integral I^{-} as function of E has been checked experimentally by using data on the charge exchange reaction $\pi^- p \to \pi^0 n$.

The importance of the latter point becomes clear from the following consideration. For the calculation of $I^-(E)$, one normally uses a simple parametrization for $\sigma^-_{hp}(E)$ of the type

$$\sigma^-_{hp}(E) = \frac{C}{E^\gamma} \quad , \tag{24}$$

where C and γ are parameters determined from a fit to experimental data on $\sigma^-_{hp}(E)$ that exist up to some maximum energy E_{max}. The critical assumption is that the above parametrization remains valid also for $E > E_{max}$. If, however, the energy dependence of $\sigma^-_{hp}(E)$ at higher energies would be different from that observed at the available energies, the result would be a nearly E-independent shift in the value of $I^-(E)$ at energies $E < E_{max}$.

However an independent determination of the integrale $I^-(E)$ can be made from charge exchange data. Requiring the πN-amplitude to be charge-independent one may derive the following expression for the forward differential cross-section of the charge-exchange reaction.

$$\frac{d\sigma}{dt}(E,t=0)_{ch.exch} = 0.102\,[\sigma^-_{\pi p}(E)]^2(1 + R^2),\ \mathrm{mb/(GeV/c)^2}, \tag{25}$$

where

$$R = I^-(E)\,\frac{\sigma_{\pi^- p}(E)}{\sigma^-_{\pi p}(E)}\ .$$

In fig. 16a are shown the values of $I^-(E)$ as obtained from the experimental data [23] on the charge exchange reaction. The solid line in fig. 16a is the result of a calculation [22] of $I^-(E)$ through the dispersion integral (23) using the following parametrization for $\sigma^-_{\pi p}$:

$$\sigma^-_{\pi p}(p) = 2.93(p/p_o)^{-0.47}, \quad p_o = 1\ \mathrm{GeV/c}. \tag{26}$$

This parametrization (HK-80/2 in ref. [22]) is the best fit to the $\sigma^-_{\pi p}$ data available in the energy range from 10 to 340 GeV (see the solid line in fig. 16b). The comparison shows that the difference between the values of $I^-(E)$ obtained using the two different methods is only of the order of 0.005. As pointed out in ref. [22], the discrepancy could be made even smaller if one applies a radiative correction to the charge exchange cross-sections.

The integral $I^+(E)$ can be calculated using eq. (22) with an uncertainty less than ± 0.01 in the energy range $10 \leq E \leq 100$ GeV [22]. This region satisfies the condition of being well above the πN-resonances, and also has a sufficient margin to the upper limit in energy $E_{max} = 340$ GeV up to which the total cross-sections have been measured. Due to the latter condition the results of the calculation are to a high degree independent on the assumptions that are made about the asymptotic behaviour of $\sigma^+_{\pi p}(E)$.

From these considerations it follows that, using the dispersion relations one can calculate $\rho_{\pi^- p}(E,t=0)$ in the energy range $10 \leq E \leq 100$ GeV with an uncertainty of at most ±0.01. Such calculations have recently been performed by Höhler et al. [22], and their results (HK-80/2) are shown in fig. 17. The experimental data on $\rho_{\pi^- p}(E,t=0)$ that were available in this energy range previously to our experiment are presented in fig. 17a. The comparison shows that the Brookhaven [24] as well as the Serpukhov [25] results deviate considerably from the predictions of the dispersion relation calculations. The deviation is particularly significant at energies around 30 GeV.

Fig. 17b shows our experimental data which were obtained in the momentum interval $30 \leq p \leq 120$ GeV/c. The point at 40 GeV/c in the same figure was obtained in an earlier measurement at Serpukhov [26] using the same experimental method. Also shown are the results at 70 GeV/c and 125 GeV/c from a recent Fermilab experiment [27]. As seen from fig. 17b, the experimental points agree with the results of the FDR calculations. The mean deviation

$$\frac{1}{N}\sqrt{\Sigma\left[\rho(p)_{\text{expt}} - \rho(p)_{\text{FRD}}\right]^2}$$ is 0.003 ± 0.004 in the energy range $30 \leq E \leq 100$ GeV. From this fact we draw the following conclusions:

i) The forward disperion relations in πp-scattering remain valid at least up to the energy of 100 GeV.

ii) The interference formula, as given by eq. (20) and the Coulomb phase determined by the equation of West and Yennie [20] are adequate for the description of the small angle πp scattering.

As to the comparison of the experimental data on $\rho_{pp}(E,t=0)$ with FDR calculations, there are two complications that, in the case of pp-scattering, might influence the accuracy of the FDR calculations. Firstly the existence of an unphysical region in the dispersion integral makes the determination of the constant C_o in eq. (21) more uncertain. Secondly there is no cross-check on the value of the integral $I^-(E)$, and the results of the FDR calculations depend to some extent on the assumptions made about the asymptotic behaviour of $\sigma^-_{pp}(E)$.

In a calculation of Grein [28], $\sigma^-_{pp}(E)$ was parametrized as

$$\sigma^-_{pp}(p) = \sigma_\omega (p/p_o)^{\alpha_\omega - 1} + \sigma_\rho (p/p_o)^{\alpha_\rho - 1} \qquad (27)$$

where $p_o = 1$ GeV/c, and the other parameters were found from a fit to the existing experimental data below 400 GeV:

$\sigma_\omega = (25.8 \pm 2.0)$ mb, $\qquad \alpha_\omega = 0.42 \pm 0.02$,

$\sigma_\rho = (1.03 \pm 0.12)$ mb, $\qquad \alpha_\rho = 0.55 \pm 0.04$.

The parameter C_o, as well as the contribution due to the unphysical region, not shown in eq. (21), was determined by Grein fitting the experimental data from ref. [29] on $\rho_{pp}(t=0)$ at $p \leq 1.7$ GeV/c. Aslo phase shift analysis data in the region $p < 1$ GeV/c were used in this fit.

The results of the calculation are shown in fig. 18 by the solid line. The dashed area corresponds to the uncertainty estimated by Grein. This uncertainty is mainly caused by the errors for the low energy data points used in the fit. In a recent experiment at Gatchina [30] new values of $\rho_{pp}(t=0)$ were obtained at $p = 1.29$ GeV/c and $p = 1.69$ GeV/c with smaller errors than those used in the fit by Grein. And yet the agreement with the calculation of Grein and the new data is quite satisfactory (see fig. 18).

It is also important that the estimated uncertainty in the calculation of ρ_{pp} decreases with energy. Therefore, one could claim that $\rho_{pp}(E,t=0)$ should be given by the FDR calculations with errors less

than ±0.01 at energies $50 \leq E \leq 400$ GeV provided however that the assumption (27) remains valid at higher energies. At energies $E > 400$ GeV the results of the calculation of ρ will depend more critically on the asymptotic behaviour of the $\sigma^+_{pp}(E)$.

The experimental data on $\rho_{pp}(t=0)$ are also presented in fig. 18. The results of the jet-target experiments at Serpukhov [31] and at Fermilab [32] made in the energy range $10 \leq E \leq 400$ GeV are in good agreement with the FDR calculations. However, recent measurements at Fermilab [27] showed deviations from dispersion relation calculations in the range 100-200 GeV. The authors of this experiment also reanalyzed the data from the jet-target experiment [32] in the energy region 200-400 GeV by introducing bigger values for b_{pp}. As a result, the ρ-values calculated from the jet- target data were shifted by $\Delta\rho=+0.04$ and then also disagree with dispersion relations. As seen in fig. 18 our data in the range 100-300 GeV do not confirm these deviations. Moreover, using values of b_{pp} that we derived from fits to all existing data on b_{pp} (see below) we obtain a shift of the jet-target data of at most $\Delta\rho = 0.02$. Finally we note that the values of $\rho_{pp}(t=0)$ found in a recent ISR experiment [36] are in good agreement with the FDR calculations.

From these considerations we conclude:

i) the existing data on $\rho_{pp}(E,t=0)$ confirm the validity of the dispersion relation in pp-scattering at least up to energies of 400 GeV,

ii) the approximation (27) used to describe the energy dependence of $\sigma^-_{pp}(E)$ at $E > 400$ GeV is compatible with the existing data on ρ_{pp}.

6.2 <u>The high energy behaviour of $\sigma^+_{\pi p}(E)$ following from the measurements of $\rho_{\pi^- p}(E,t=0)$</u>.

In our previous discussion we concluded that the forward dispersion relations for πp-scattering are valid at energies at least up to $E = 100$ GeV. Assuming the validity of the FDR also at energies above 100 GeV and using the values of $\rho_{\pi^- p}(t=0)$ measured at energies up to $E = 345$ GeV we can probe the energy dependence of $\sigma^+_{\pi p}(E)$ at energies above 345 GeV.

In the case of pp-scattering, such a program has been fulfilled by the CERN-Rome collaboration [33]. This group has measured $\rho_{pp}(E,t=0)$ in the energy range $500 < E < 2000$ GeV (see fig. 18), and a simultaneous fit to the available experimental data on $\rho_{pp}(E,t=0)$ and $\sigma_{p\pm p}(E)$ was performed. The following parametrization of the total cross-section was used:

$$\sigma^{+}_{pp}(E) = \sigma_o + \sigma_1 (E/E_o)^{\alpha_1 - 1} + \sigma_2 [\ln(s/s_o)]^a , \tag{28}$$

$$\sigma^{-}_{pp}(E) = C(E/E_o)^{\alpha_2 - 1} , \tag{29}$$

where $E_o = 1$ GeV and $s_o = 1$ GeV^2.

From the fit, the following values of the constants entering eqs. (28) and (29) were obtained:

$\sigma_o = (27.0\pm1.0)$mb, $\sigma_1 = (41.9\pm1.1)$mb,

$\sigma_2 = (0.17\pm0.08)$mb, $C = (24.4\pm1.1)$mb,

$\alpha_1 = 0.63\pm0.03$, $\alpha_2 = 0.45\pm0.02$, $a = 2.1\pm0.1$.

This analysis led to a remarkable conclusion: the rise in $\sigma^{+}_{pp}(E)$, as described by eq. (28), continues at least up to 40 000 GeV. At this energy, the total cross section should reach the value of about 56 mb which exceeds by 35% the value of $\sigma^{+}_{pp}(E)$ at $E = 100$ GeV.

An analogous investigation in the case of π^-p-scattering represents an alternative way of exploring the asymptotic region of hadronic interactions. The energies at the SPS are smaller than those at the ISR; however on the other hand there are several indications that the asymptotic region in πp-interactions starts earlier than in pp-interactions [7].

Figs. 19 and 20 present the available experimental data on $\sigma^{\pm}_{\pi p}$ and $\rho_{\pi^- p}(t=0)$. In a first attempt to analyze the data [9], we used the already mentioned parametrization HK-80/2 of $\sigma^{\pm}_{\pi p}$ proposed by Höhler et al. [22]:

$$\sigma^{+}_{\pi p} = \sigma_o + \sigma_1 (p/p_o)^{\alpha_1 - 1} + \sigma_2 \, [\ln (p/p_1)]^2, \tag{30}$$

$$\sigma^{-}_{\pi p} = C(p/p_o)^{\alpha_2 - 1} \tag{31}$$

with the values of the constants found from the best fit to the experimental data on $\sigma_{\pi \pm p}$:

$\sigma_o = 22.26$ mb, $\sigma_1 = 8.23$ mb, $\sigma_2 = 0.42$ mb,

$C = 2.93$ mb, $\alpha_1 = 0.53$, $\alpha_2 = 0.53$,

$p_1 = 37.8$ GeV/c, $p_o = 1$ GeV/c (fixed).

The dash-dotted curve in fig. 19 demonstrates the high energy behaviour of $\sigma_{\pi - p}(E)$ given by the eqs. (30) and (31). The corresponding ρ-values calculated through the forward dispersion relations are shown in fig. 20 (dash-dotted line). From the figure it is seen that starting from about 150 GeV and going to higher energies the calculated ρ-values deviate systematically from the experimental data.

In the next step, we have performed a simultaneous fit to the σ_{tot} data and to the $\rho_{\pi - p}$ data shown in figs. 19 and 20 using the following parametrization:

$$\sigma^{+}_{\pi p}(E) = \sigma_o + \sigma_1 (E/E_o)^{\alpha_1 - 1} + \sigma_2 \, [\ln(E/E_1)]^a, \tag{32}$$

$$\sigma^{-}_{\pi p}(E) = C(E/E_o)^{\alpha_2 - 1}, \tag{33}$$

In this analysis, the value of the scale factor E_1 was fixed to be that of the pion mass, $E_1 = m_\pi$. On the other hand, the power of the logarithmic term was left as a free parameter. Such an approach is similar to that of the ISR group in their analysis of the pp-data (compare eqs. (28) and (32)). The results obtained from our fit are:

σ_o = (12.28±1.0)mb, σ_1 = (24.13±0.24)mb, σ_2 = (0.09±0.03)mb,

C = (2.83±0.14)mb, α_1 = 0.67±0.03, α_2 = 0.55±0.01,

E_o = 1 GeV (fixed), a = 2.24±0.13, E_1 = 140 MeV (fixed).

The calculated ρ-values are shown in fig. 20 by the dotted line. As seen from the figure, this line fits well all the experimental points except the last point at 345 GeV/c. The overall agreement can be further improved by introducing a break parameter E_{break} which is the energy where $\sigma^+_{\pi p}$ would be allowed to flatten out to a constant level. The best fit is achieved for

$$E_{break} = 4000\ ^{+9000}_{-1800}\ (^{+\infty}_{-2500})\ \text{GeV}.$$

where the values in brackets correspond to two standard deviation of the break parameter. The corresponding curves for $\sigma_{\pi^\pm p}$ and $\rho_{\pi^- p}$ are shown in figs. 19 and 20 (full lines).

In conclusion, the obtained data are consistent with the assumption of a total πp cross-section that continues to rise with energy at least up to 2000 GeV. At this energy, the total cross-section should reach the value of about 29 mb which exceed by ∿ 20% the value of $\sigma^+_{\pi p}(E)$ at E ≃ 70 GeV. The experimental data do not exclude the possibility that the rise of $\sigma^+_{\pi p}$ with energy continues indefinitely. However, in this case the rise in the region 1000-10000 GeV must be slower than what follows from the parametrization HK-80/2.

The comparison of the results from the present experiment with the results of the ISR group reveals a close similarity in the high energy behaviour of πp and pp interactions. This may in turn be taken as an indication of that the rise of the total cross-sections is a universal feature of hadronic interactions.

The main prediction of the classical Pomeron theory [2] was that the total hadronic cross-section become constant at asymptotically high energies. This theory admitted some slow rise of σ_{tot} in the preasymptotic s-region caused by the logarithmic decrease of the contribution due to exchanges by two Pomerons. However, within the framework of this theory,

it seems difficult to explain the high rate of increase with energy of $\sigma_{pp}(E)$ and $\sigma_{\pi p}(E)$. Therefore, the further development of alternative approaches like the "Critical Pomeron" theory or the "Supercritical Pomeron" theory as discussed for example by White in a recent publication [40] seems to us important.

It is interesting to compare the observed rise in σ_{tot} with the Froissart bound. Let us assume that the asymptotic behaviour of $\sigma^{+}_{pp}(s)$ and $\sigma^{+}_{\pi p}(s)$ is given by eqs. (28) and (32):

$$\sigma_{pp}(s\to\infty) = (0.17\pm0.08)\left[\ln(s/s_{op})\right]^{2.1\pm0.1}\ \text{mb}$$

$$\sigma_{\pi p}(s\to\infty) = (0.09\pm0.03)\left[\ln(s/s_{o\pi})\right]^{2.24\pm0.13}\ \text{mb}$$

where $s_{op} = 1\ \text{GeV}^2$ and $s_{o\pi} = 2m_p m_\pi = 0.26\ \text{GeV}^2$.

The Froissart limit may be expressed by the formula:

$$\sigma_{tot}(s\to\infty) \leq \sigma^* [\ln(s/s_o)]^2, \tag{34}$$

$$\sigma^* \leq \pi(N-1)^2/m_\pi^2, \tag{35}$$

where s_o is an arbitrary scale constant and N determines the maximum possible rise of the scattering amplitude:

$$F(s,t) \leq (s/s_o)^N \quad (s\to\infty) \tag{36}$$

From field theory it follows that $N\leq 2$. With N=2, eq. (35) gives $\sigma^* \leq 60$ mb. Eq. (35) is established for pp-scattering, while in the πp case a weaker limit was set so far: $\sigma^* \leq 12\pi/m_\pi^2$ [41]. As seen from the comparison, the experimental values of the power of the logarithmic term are close to the Froissart limit (a = 2). On the other hand, the values of the coefficient of the logarithmic term are more than by two orders of magnitude under the Froissart bound $\sigma^* = 60$ mb.

Such a big difference cannot be explained only by unsufficient saturation of the unitary limit. This means that in eq. (35) either N is close to 1 or the mass of the exchange systeme is larger than the π mass.

6.3 The possibility of universal shrinkage of the hadronic diffraction cone

The classical Pomeron theory gives in first approximation the following expression for the elastic differential cross-section at asymptotically high energies:

$$\frac{d\sigma_{ij}}{dt} \sim s^{2(\alpha_p(t)-1)} \tag{37}$$

where $\alpha_p(t)$ is a Regge trajectory. If $\alpha_p(t)$ is linear i.e. $\alpha_p(t) = \alpha_p(o) + \alpha_p' t$, then for the slope b using the definition

$$b_{ij} = d/dt\ [\ln(d\sigma/dt)] \tag{38}$$

we obtain

$$b_{ij} \sim 2\alpha_p' \ell ns \tag{39}$$

and thus

$$\frac{db_{ij}}{d(\ell ns)} \sim 2\alpha_p' \tag{40}$$

In this case there should be "universal shrinkage" of the diffraction cone which should not depend on the kind of the incident hadron and on the t-values.

Until now it was generally thought that "true" Pomeron shrinkage showed up only in pp-scattering at small t-values where the shrinkage parameter was reported [4] to be

$$2\alpha_p' = (0.556 \pm 0.048)\ (GeV/c)^{-2}.$$

This unique feature of the pp-slope was sometimes explained as being due to the mutual cancellation of the ω and f amplitudes which allowed the Pomeron contribution to dominate already at small energies.

Below, we present the analysis of the results from the present experiment together with the existing world data on elastic slopes. It will be shown that the available data are consistent with a universal shrinkage of the hadronic diffraction cone. The value of the shrinkage parameter is $2\alpha_p' = 0.28\ (GeV/c)^{-2}$ which is a factor of 2 less than the value mentioned above.

Let us consider first the data of $\pi^- p$ scattering. The values of the slope parameter b obtained in our experiment are presented in fig. 21. The

data available in π^-p scattering obtained in other experiments in the t-region close to t=0 are also shown in the figure. Our data and the data of Fajardo et al. [27] in the energy range 70-200 GeV agree reasonably well. From the b-data of Foley et al. [24] we have included only those energy points for which the measurements of $\rho_{\pi^-p}(t=0)$ are consistent with the values given by dispersion relations (see fig. 17). We have imposed this consistency condition of the data in particular as there is a correlation between ρ and b when fitting the data. In the experiment of Russ et al. [42] the minimum t-value was $-t = 0.05$ $(GeV/c)^2$. We have extrapolated to $-t = 0.02$ $(GeV/c)^2$ using the t-dependence suggested by the authors themselves. Fig. 21 also shows our compilation of the world data at $-t = 0.2$ $(GeV/c)^2$ and $-t = 0.4$ $(GeV/c)^2$. Details of this compilation can be found in ref. [16].

In our first analysis [9] the data on b_{π^-p} were fitted with the following parametrization

$$b(p) = b_o + 2\alpha'_p \ln p \tag{41}$$

The values of $2\alpha'_p$ found were

(0.23 ± 0.04) $(GeV/c)^{-2}$ at $-t = 0.02$ $(GeV/c)^2$,

(0.22 ± 0.02) $(GeV/c)^{-2}$ at $-t = 0.2$ $(GeV/c)^2$,

(0.19 ± 0.03) $(GeV/c)^{-2}$ at $-t = 0.4$ $(GeV/c)^2$

From these data, it was concluded that there is shrinkage of the π^-p-diffraction cone at all three t-values, and that within errors the shrinkage parameter is independent of t.

In fig. 21 are also presented our data on b_{pp} [10] togeter with data from other small angle experiments, corrected if necessary for t-dependence to correspond to the same t-value, i.e. $-t = 0.02$ $(GeV/c)^2$. Note the good agreement of our points with those of Fajardo et al [27].

On the other hand, our data disagree in the absolute scale with the jet-target data of ref. [3]. The disagreement is of the order of $\Delta b = 0.4$ $(GeV/c)^{-2}$ after the correction for the t dependence has been applied.

Also shown in fig. 21 are the world data on b_{pp} at $-t = 0.2$ (GeV/c)^2 and $-t = 0.4$ (GeV/c)^2. Fig. 22 presents our compilation [16] of the world data on $b_{\pi^{\pm}p}$, $b_{K^{\pm}p}$, and $b_{p^{\pm}p}$ at $-t = 0.2$ (GeV/c)^2.

It is apparent from figs. 21 and 22 that the data on slope parameters do not follow straight lines when plotted as function of ln p. We were thus led to introduce an additional term in eq. (41) to take into account also the nonlogarithmic part of the p-dependences of the slopes:

$$b(p) = b_o + b_1(p/p_o)^{-q} + b_2 \cdot \ln(p/p_o), \qquad (42)$$

where $p_o = 1$ GeV/c.

This parametrization is compatible to first order with the Regge pole model, where the new term represents the interference between the Pomeron and secondary trajectories. Surprisingly enough we have found that the suggested parametrization fits well all the data shown in figs. 21 and 22. The results are presented in table 7. The data at $-t = 0.2$ (GeV/c)^2 were fitted simultaneously for particles and antiparticles with four free parameters (b_1 was allowed to be different for particles and antiparticles). In the cases of p/p^- and K^+/K^- it was also possible to make fits with five free parameters, including the parameter q. While fitting the data on $b_{pp}(-t = 0.02$ (GeV/c)$^2)$, the absolute scale of the experimental points from ref. [3] was left free. The solid lines in figs. 21 and 22 show the slopes calculated using eq. (42) with the fitted parameters listed in table 7, and the dashed lines in fig. 22 represent the part of eq. (42) that is linear in lnp. Note the remarkably good values of χ^2/NDF in all the fits which is somewhat unexpected, taking into account the simple form of the parametrization and the big p-range used in the fits.

The asymptotic shrinkage parameters were found to have nearly the same value for all particles, and this value does not seem to depend on the momentum transfer in the t-range $|t| \leq 0.2$ (GeV/c)^2:

$$\langle b_2 \rangle \equiv 2\alpha'_p = (0.28 \pm 0.03)\ (\text{GeV/c})^{-2}.$$

The results have been checked for stability. For example, if we take away all the $\bar{p}/p$ points below 10 GeV we obtain for $-t = 0.2$ (GeV/c)^2

$$b_2(pp) = (0.26 \pm 0.08)\ (\text{GeV/c})^{-2}.$$

For small angle pp-scattering $b_2 = (0.30\pm0.04)\ (GeV/c)^{-2}$ which is different from the value $2\alpha'_p = (0.56\pm0.05)\ (GeV/c)^{-2}$ found previously [3]. The difference is due to the introduction of the non linear term $b_1(p/p_o)^{-q}$ in conjunction with our experimental data together with the recent data from Fermilab. Table 7 shows that this term is important in the pp case.

We conclude that the present experimental data on slopes at $-t \leq 0.2$ $(GeV/c)^2$ are well fitted by parametrization (42). The data are also consistent with the hypothesis of universal shrinkage of the hadronic diffraction cone at high energies, the value of the asymptotic shrinkage parameter being $2\alpha'_p = (0.28\pm0.03)\ (GeV/c)^{-2}$. This latter conclusion depends of course on the parametrization used, but the good quality of the fits shows that it cannot be changed on the basis of statistical criteria only.

As a consequence of eq. (42), the difference in the diffraction cone slopes for antiparticles and particles is given as

$$b_{h^-p} - b_{h^+p} = \text{const.}\ (p/p_o)^{-q}. \tag{43}$$

From this equation, it follows that $b_{h^-p} = b_{h^+p}$ at $p \to \infty$ in accordance with the theorem of the asymptotic equality of the differential cross-sections for scattering of antiparticles and particles [49].

It is interesting to point out a similarity of eq. (43) to the expression describing the difference in the total cross-sections:

$$\sigma_{h^-p} - \sigma_{h^+p} = \text{const.}\ (p/p_o)^{-\gamma}. \tag{44}$$

Comparing the values for q obtained in our fits to the slopes at $-t = 0.2$ $(GeV/c)^2$ (see table 7) with the values for the γ-parameter published in literature, we have:

p^-p :	$q = 0.52\pm0.02$,	$\gamma = 0.55\pm0.02$	[33]
K^-K^+ :	$q = 0.56\pm0.03$,	$\gamma = 0.56\pm0.03$	[21]

Such a close similarity in the behaviour of the differences of the total cross-sections and slopes (natural in the naive diffraction model) does not have straightforward explanation in the Regge pole model.

6.4 On the t-dependence of the slope parameters

The data in fig. 21 show that the slope parameter has a non-linear dependence on the four-momentum transfer squared t. The most detailed information, over a large t-range, of the t-dependance of b was obtained in recent experiments by Schiz et al., [50] on pp and πp scattering at 200 GeV and by Russ et al., [42] on πp scattering at 8 GeV/c and 16 GeV/c (see fig. 23). The numbers of collected events in these experiments were high enough to make possible a determination of b in several limited t-regions within the t-range up to $-t = 0.5$ (GeV/c)^2.

In fig. 23 are also shown the results of the analysis of the NA8 data obtained in the following way. In order to increase the total statistics, we fitted simultaneously all the differential cross sections measured at different momenta p, introducing as p dependance of the slopes a parametrization according to equation (42). In this case it was possible to obtain significant results also when subdividing our t-region into the two regions $0.002 \leq -t \leq 0.02$ (GeV/c)^2 and $0.02 \leq -t \leq 0.04$ (GeV/c)^2 making independent determinations of b in each of these two regions. The experimental points in fig. 23 were fitted using the following parametrization:

$$b(t) = b_o - 2c|t| + 3d|t|^2.$$

The results of the fits are shown in fig. 23 by solid lines and the parameters obtained in the fits are given in table 8.

Fig. 23 shows that the fall-off of the slope parameter with t is quite similar for the different particles and energies, a fact which may be taken as a further indication of the universal behaviour of hadronic interactions at high energies. As already discussed in ref. [27], the observed t-dependence of the differential cross sections can be well fitted with a parametrization [51,52] based on the Additive Quark Model (AQM):

$$\frac{d\sigma}{dt} hp\ (s,t) \propto G_h^2(t)\ G_p^2(t)|Aqq\ (s,t)|^2$$

where

$G_h(t)$ is either of the hadron form factors:

$$G_\pi(t) = [1 - r_\pi^2 t/6\hbar^2]^{-1}$$

or

$$G_p(t) = [1 - r_p^2 t/12\hbar^2]^{-2}$$

and $A_{qq}(s,t) = \exp \frac{r_q^2(s)t}{4\pi^2}$ is the quark-quark scattering amplitude and r_π, r_p and r_q are the r.m.s. radii of the pion, the proton and the "dressed" quark respectively.

The dashed line in fig. 23 shows b(t) as obtained in ref. [50] using the AQM parametrization with the values of r_π, r_p and r_q obtained from a fit to the measured πp differential cross-section at 200 GeV/c. The agreement of the AQM curve with the data is quite satisfactory. However the t-dependence in this AQM parametrization is dominated by the form factors, therefore other models [53] containing these form factors may equally well fit the data.

Sincere thanks and recognition are due to those who, at CERN and at our home laboratories, helped us in fulfilling the research program described in this paper.

REFERENCES

[1] M.L. Goldberger et al., Phys. Rev. 99 (1955) 986;
N.N. Bogoljubov, Intern. Conf. on Theor. Phys., Seatle, USA (1956);
K. Symanzik, Intern. Conf. on Theor. Phys., Seatle, USA (1956).

[2] T. Regge, Nuovo Cimento 14 (1959) 951 and 18 (1960) 947;
V.N. Gribov, JETP 41 (1961) 667, 41 (1961) 1962 and 42 (1962) 1250;
V.N. Gribov and I.Y. Pomeranchuk, Phys. Rev. Lett. 8 (1962) 343 and 8 (1962) 412.

[3] V.D. Bartenev et al., Phys. Rev. Lett. 31 (1973) 1088.

[4] G. Giacomelli, Phys. Rep. 23C (1976) 123.

[5] J.P. Burq et al., Phys. Lett. 77B (1978) 438.

[6] J.P. Burq et al., Nucl. Instr. 177 (1980) 353.

[7] J.P. Burq et al., CERN Int. Rep. 78-07 (1978).

[8] J.P. Burq et al., Nucl. Phys. B187 (1981) 205.

[9] J.P. Burq et al., Phys. Lett. 109B (1982) 111.

[10] J.P. Burq et al., Phys. Lett. 109B (1982) 124.

[11] J.V. Allaby and C. Bovet, Monitoring of SPS secondary beams, CERN,/LabII/EA/74-5 (1974).

[12] C. Bovet et al., The CEDAR PROJECT, CERN/LabII/EA/74-4.

[13] A.A. Vorobyov et al., Report LNPI No 429 (1972).

[14] A.A. Vorobyov et al., Nucl. Instr. 119 (1974) 509.

[15] S.A. Baranov et al., Yad. Fiz. 5 (1967) 518.

[16] J.P. Martin, Thesis PhD, Lyon (1981).

[17] A.P. Kashchuk et al., Report LNPI No 395 (1978).

[18] M. Sogard, Phys. Rev. D9 (1974) 1486.

[19] M.M. Nagels et al., Nucl. Phys. B109 (1976) 1.

[20] G.B. West and D.R. Yennie, Phys. Rev. 172 (1968) 1413.

[21] A.S. Carroll et al., Phys. Lett. 61B (1976) 303 and 80B (1979) 423.

[22] G. Höhler et al., Phys. Lett. 58B (1975) 348;
Karlsruhe preprint KFK 2457 (1977);
Karlsruhe preprint TKP 80-14 (1980).
G. Höhler: Pion-Nucleon Scattering. Vol. I (Tables of Data) and Vol. II (Methods and results of phenomenological analyses). Landolt-Börnstein Vols. I/9b1 and 2. Springer-Verlag, Heidelberg.

REFERENCES (Cont'd)

[23] A.V. Barnes et al., Phys. Rev. Lett. 37 (1976) 76.

[24] K.J. Foley et al., Phys. Rev. 181 (1969) 1775.

[25] V.D. Apokin et al., Soviet J. Nucl. Phys. 25 (1977) 51;
Phys. Lett. 56B (1975) 391 and Nucl. Phys. B106 (1976) 413.

[26] V.G. Ableev et al., Yad. Fiz. 28 (1979) 1529.

[27] L.A. Fajardo et al., Phys. Rev. D24 (1981) 46.

[28] W. Grein, Nucl. Phys. B131 (1978) 1975.

[29] A.A. Vorobyov et al., Phys. Lett. 41B (1972) 639.

[30] G.N. Velichko et al., Report LNPI No 656 (1981).

[31] G.G. Beznogikh et al., Phys. Lett. 39B (1979) 411.

[32] D. Gross et al., Phys. Rev. Lett. 41 (1978) 217.

[33] U. Amaldi et al., Phys. Lett. 66B (1977) 390.

[34] K.J. Foley et al., Phys Rev. Lett. 19 (1967) 857.

[35] P. Jenni et al., Nucl. Phys. B129 (1977) 232.

[36] D. Favart et al., Phys. Rev. Lett. 47 (1981) 1191.

[37] G. Von Dardel et al., Phys. Rev. Lett. 8 (1962) 173.

[38] K.J. Foley et al., Phys. Rev. Lett. 19 (1967) 330.

[39] S.P. Denisov et al., Phys. Lett. 36B (1971) 415 and 36B (1971) 528;
Nucl. Phys. B65 (1973) 1, and Yad. Fiz. 15 (1972) 953.

[40] A.R. White, preprint FERMILAB-Conf-81/16-THY, January 1982.

[41] A.G. Eden, "High energy collision of elementary particles",
Cambridge University Press 1967.

[42] J.S. Russ et al., Phys. Rev. D15 (1977) 3139.

[43] G.G. Beznogikh et al., Phys. Lett. 43B (1973) 85.

[44] U. Amaldi et al., Phys. Lett. 36B (1971) 504.

[45] G. Barbiellini et al., Phys. Lett. 39B (1972) 663.

[46] L. Baksay et al., Nucl. Phys. B141 (1978) 1.

[47] K.M. Chernev et al., Phys. Lett. 36B (1971) 266.

REFERENCES (Cont'd)

[48] G. Belletini et al., Phys. Lett. 14 (1965) 164.

[49] A.A. Logunov et al., Phys. Lett. 7 (1963) 69;
L. Van Hove, Phys. Lett. 5 (1963) 252 and 7 (1963) 76.

[50] A. Schiz et al., Phys. Rev. D24 (1981), 26.

[51] A. Bialas et al., Acta Physica Polonica, B8 (1977) 855.

[52] E.M. Levin and V.M. Skekhter, Leningrad Report No 442, 1978.

[53] T.T. Chou and C.N. Yang, Phys. Rev. 170 (1968) 1591;
J.J. Kokkedee and L. Van Hove, Nuovo Cimento, 42 (1966) 711.

[54] D.S. Ayres et al.
Phys. Rev. D15(1977) 3105.

[55] C.W. Akerlof et al.
Phys. Rev. D14(1976) 2864.

TABLE 1

Beam composition and the mean absolute momentum. Lepton contaminations are the upper limits estimated at the beam stopper position

Polarity	p_o Nominal momentum, GeV/c	p* Absolute momentum, GeV/c	Beam content at CEDAR position %			Lepton contamination, %	
			$\pi+\mu+e$	K	p	μ/π	e/π
-	100	100.30±0.05	93.50	4.10	2.40	2.34	2.06
+	100	100.20±0.05	62.40	3.00	34.60	1.90	0.70
-	150	150.52±0.18	94.10	4.72	1.18	1.98	1.32
+	150	150.52±0.08	41.80	4.70	53.50	1.45	0.10
-	200	200.79±0.12	96.50	2.83	0.67	2.00	-
-	250	250.38±0.13	97.30	2.44	0.26	2.00	-
+	250	250.38±0.18	7.50	0.70	91.80	1.90	-
-	280	280.64±0.28	98.75	1.15	0.10	1.78	-
-	300	299.88±0.18	99.00	0.92	0.08	1.80	-
+	300	299.76±0.18	1.75	0.35	97.90	1.80	-
-	325	-	99.60	0.40	-	1.80	-
-	345	-	99.87	0.13	-	1.80	-

TABLE 2

The accuracy in measurements of different quantities

Measured quantity	Notation	Precision (standard deviation)
Incident particle momentum	p	$\sigma(p)/p = 0.05\%$
Scattered particle momentum	p'	$\sigma(p')/p' = (0.2 \div 0.3)\%$
Forward scattering angle	θ	$\sigma_{\theta proj} = 30$ μrad at 100 GeV/c $\sigma_{\theta proj} = 18$ μrad at 300 GeV/c
Energy deposited on anode A	T_A	$\sigma(T_A) = 50$ KeV
Energy deposited on anode B	T_B	$\sigma(T_B) = 50$ KeV
Energy deposited on anode C	T_C	$\sigma(T_C) = 40$ KeV
Analog sum of T_A and T_B	T_{AB}	$\sigma(T_{AB}) = 70$ KeV
Delay of cathode signal	t_K	$\sigma(t_K) = (0.4 \div 0.1)\mu s$ at $T_{AB} = (1 \div 5)$ MeV
Delay of anode A signal	t_A	$\sigma(t_A) = 60$ ns at $T_A > 0.5$ MeV
Delay of anode B signal	t_B	$\sigma(t_B) = 60$ ns at $T_B > 0.5$ MeV
x-coordinate of the vertex	x_r	$\sigma(x_r) = 0.15$ mm
y-coordinate of the vertex	y_r	$\sigma(y_r) = 0.15$ mm
z-coordinate	z_r	$\sigma(z_r) = 0.3$ mm
Recoil track projection on the beam axis	X_r	$\sigma(X_r) = (3 \div 1.5)$ mm at $T_{AB} = (1 \div 5)$ MeV

TABLE 3

Test events elimination by different criteria
and global inefficiency at 250 GeV/c (negative beam)

Reasons for test events elimination	Percentage of rejected test events
Muons	2.00
Electrons	-
Reconstruction of the forward particle track is impossible	1.10
Incoming trajectory does not provide full geometrical acceptance	2.00
The momentum of the scattered particle is outside ± 5% of the incident beam momentum	0.20
More than one IKAR cell has V_A and V_{AB} amplitudes higher than levels of the digital discriminator	1.40
Showers detected by A3 counters in coincidence with cathode pulse	6.50
Global inefficiency	13.20 %

TABLE 4

Estimated contributions to the normalization error

The source of an error	The estimated value, %
Absolute t-scale	0.5
Inefficiency and background	0.4
Effective target length	0.4
Gas density	0.1

TABLE 5

Differential cross-sections for $\pi^- p$ and pp elastic scattering. The errors are statistical and represent one standard deviation, the absolute normalization error is 1%. Only results of NA8 experiment are presented. The tables for WA9 experiment can be found in ref. [7].

|t| (GeV/c)^2	dσ/dt mb/(GeV/c)^2	ERROR mb/(GeV/c)^2
.0022	84.4043	2.1971
.0023	76.2488	2.0617
.0025	71.0007	1.9743
.0027	64.9349	1.8791
.0029	59.5229	1.7940
.0031	60.9112	1.8117
.0033	54.1355	1.7063
.0035	50.0564	1.6397
.0037	49.1914	1.6249
.0038	46.6146	1.5815
.0040	41.2643	1.4878
.0042	42.8699	1.5164
.0044	42.8478	1.5160
.0046	40.3792	1.4716
.0048	37.4687	1.4176
.0050	40.7611	1.4786
.0052	37.0952	1.4105
.0053	37.5941	1.4200
.0055	35.9036	1.3877
.0057	36.5175	1.3995
.0059	36.9006	1.4068
.0061	36.4323	1.3979
.0063	34.7680	1.3656
.0065	34.0956	1.3523
.0067	33.4020	1.3385
.0068	33.1800	1.3340
.0070	32.7942	1.3263
.0072	35.5018	1.3815
.0074	32.2702	1.3156
.0076	30.4374	1.2778
.0078	33.4005	1.3385
.0080	31.6991	1.3040
.0082	31.2970	1.2957
.0084	32.2693	1.3157
.0085	29.9484	1.2676
.0087	32.3119	1.3167
.0091	28.9022	.7178
.0097	29.1279	.7190
.0102	28.0979	.7050
.0108	28.3391	.7076
.0114	29.1057	.7172
.0119	27.5406	.6978
.0125	27.6421	.6993
.0130	26.9791	.6911
.0136	25.3646	.6703
.0143	26.1727	.5899
.0150	26.6322	.5952
.0158	26.1256	.5897
.0165	26.0238	.5887
.0173	24.1617	.5673
.0180	25.9523	.5800
.0188	23.9869	.5653
.0195	24.3509	.5697
.0203	23.5868	.5606
.0210	24.5518	.5719
.0218	24.6913	.5734
.0226	24.4865	.5106
.0236	23.9087	.5043
.0245	23.4827	.4996
.0254	22.8892	.4930
.0264	22.1890	.4850
.0273	23.2452	.4961
.0282	22.2804	.4853
.0292	21.9288	.4810
.0301	20.5124	.4647
.0311	21.1206	.4710
.0321	21.3906	.4321
.0332	21.1360	.4288
.0343	20.8406	.4251
.0355	20.4661	.4205
.0366	20.0597	.4155
.0377	20.0722	.4147
.0388	20.3056	.4162

TABLE PI-H -100 GEV

T	SIGMA MB/(GEV**2)	ERROR
.0022	85.5220	1.9141
.0023	77.1948	1.8028
.0025	69.4061	1.7014
.0027	63.6867	1.6258
.0029	60.2744	1.5797
.0031	59.3885	1.5673
.0033	55.6124	1.5163
.0035	49.9528	1.4371
.0037	49.9923	1.4378
.0038	49.7645	1.4346
.0040	45.9774	1.3791
.0042	43.2024	1.3369
.0044	40.7085	1.2978
.0046	42.8307	1.3312
.0048	39.8845	1.2846
.0050	39.6836	1.2814
.0052	37.9076	1.2523
.0053	35.9460	1.2195
.0055	35.7933	1.2168
.0057	35.7770	1.2165
.0059	36.9661	1.2365
.0061	34.3683	1.1923
.0063	34.7918	1.1995
.0065	35.6776	1.2147
.0067	33.9103	1.1842
.0068	33.6030	1.1788
.0070	32.7778	1.1642
.0072	30.9002	1.1303
.0074	33.0832	1.1695
.0076	30.6121	1.1250
.0078	32.0902	1.1518
.0080	32.2590	1.1549
.0082	31.6021	1.1430
.0084	31.0990	1.1404
.0085	32.1700	1.1534
.0087	31.3062	1.1377
.0091	30.7683	.6506
.0097	30.6053	.6483
.0102	29.9419	.6405
.0109	28.2253	.5382
.0116	28.3796	.5396
.0124	27.6192	.5324
.0131	27.5552	.5319
.0139	27.4062	.5305
.0146	27.2285	.5289
.0154	26.4713	.5216
.0162	26.3354	.4654
.0172	25.8625	.4613
.0181	25.8270	.4611
.0190	24.5879	.4500
.0200	24.7681	.4517
.0209	25.7404	.4605
.0219	24.6395	.4506
.0228	23.6836	.4418
.0238	24.0729	.4066
.0250	24.3289	.4088
.0261	23.6520	.4030
.0272	22.7371	.3951
.0283	22.9481	.3969
.0295	21.9754	.3883
.0306	21.6857	.3857
.0318	22.0312	.3598
.0331	21.5806	.3559
.0344	20.9832	.3508
.0357	21.0680	.3513
.0371	21.0585	.3510
.0384	20.5248	.3463
.0392	20.0246	.6397

TABLE PI-H -150 GEV

TABLE 5 (cont'd)

T	SIGMA MB/(GEV**2)	ERROR
.0022	85.9283	1.8468
.0023	79.9406	1.7668
.0025	72.9861	1.6811
.0027	68.4787	1.6243
.0029	61.4812	1.5372
.0031	57.1647	1.4816
.0033	53.8554	1.4379
.0035	53.7291	1.4362
.0037	49.3917	1.3772
.0038	48.0608	1.3587
.0040	46.3998	1.3351
.0042	45.8844	1.3278
.0044	43.6154	1.2947
.0046	41.6796	1.2657
.0048	39.9130	1.2387
.0050	41.2670	1.2595
.0052	40.3561	1.2456
.0053	39.3979	1.2307
.0055	36.1405	1.1787
.0057	38.1916	1.2117
.0059	35.6760	1.1711
.0061	38.6845	1.2195
.0063	38.4755	1.2161
.0065	37.5262	1.2010
.0067	34.8102	1.1567
.0068	35.3932	1.1663
.0070	34.3955	1.1498
.0072	33.7329	1.1386
.0074	31.6757	1.1034
.0076	35.4492	1.1672
.0078	32.8501	1.1236
.0080	33.8865	1.1412
.0082	31.3626	1.0979
.0084	33.0621	1.1272
.0085	32.4206	1.1162
.0087	32.2364	1.1131
.0092	32.8636	.5612
.0099	31.1728	.5450
.0107	30.8067	.5410
.0114	29.3773	.5282
.0122	27.8451	.5143
.0129	28.0076	.5160
.0137	28.5870	.5215
.0145	27.4977	.4576
.0155	27.5203	.4580
.0164	27.1718	.4553
.0174	27.9940	.4622
.0183	27.1161	.4551
.0192	25.8784	.4446
.0202	25.5094	.4415
.0212	24.7932	.3974
.0223	24.8557	.3979
.0235	24.8767	.3981
.0246	24.0750	.3916
.0257	24.1845	.3924
.0268	23.9080	.3901
.0281	23.0543	.3545
.0294	22.9503	.3535
.0307	22.6658	.3511
.0320	22.4018	.3468
.0333	22.1190	.3463
.0346	21.9070	.3443
.0359	21.1792	.3381
.0373	20.9453	.3141
.0388	20.9503	.3354

TABLE PI-H -200 GEV

T	SIGMA MB/(GEV**2)	ERROR
.0022	87.7965	2.5095
.0023	82.5460	2.4086
.0025	73.0712	2.2525
.0027	67.3919	2.1558
.0029	63.8619	2.0941
.0031	57.6444	1.9873
.0033	54.8469	1.9376
.0035	55.1305	1.9424
.0037	51.4142	1.8758
.0038	50.1206	1.8522
.0040	50.9017	1.8669
.0042	47.6251	1.8061
.0044	45.3648	1.7629
.0046	43.1798	1.7201
.0048	40.9245	1.6748
.0050	42.6448	1.7098
.0052	40.8248	1.6730
.0053	40.1733	1.6597
.0055	39.9226	1.6546
.0057	39.4104	1.6440
.0059	38.6632	1.6283
.0061	35.3870	1.5578
.0063	40.0826	1.6580
.0065	39.5678	1.6473
.0067	36.1055	1.5735
.0068	37.5745	1.6052
.0070	36.3492	1.5788
.0072	36.0795	1.5729
.0074	31.9563	1.4803
.0076	34.3020	1.5337
.0078	31.7659	1.4759
.0080	31.9208	1.4794
.0082	32.7011	1.4974
.0084	35.4257	1.5585
.0085	36.4834	1.5816
.0087	36.3556	1.5788
.0093	31.6065	.6564
.0102	30.6866	.6449
.0112	30.9022	.6462
.0121	29.3558	.6296
.0130	29.1364	.6274
.0141	28.2045	.5636
.0152	28.0513	.5623
.0163	27.4362	.5562
.0175	27.3546	.5555
.0187	26.9214	.5103
.0200	25.9260	.5008
.0213	25.6709	.4984
.0226	24.9873	.4917
.0240	24.8616	.4588
.0255	24.6628	.4568
.0270	24.7151	.4571
.0285	23.9582	.4499
.0301	23.1235	.4164
.0318	23.3513	.4181
.0335	22.6258	.4112
.0352	21.7363	.4026
.0370	21.4007	.3784
.0387	21.4542	.4230

TABLE PI-H -250 GEV

TABLE 5 (cont'd)

T	SIGMA MB/(GEV**2)	ERROR
.0022	89.8590	2.1354
.0023	83.7732	2.0343
.0025	73.1735	1.8862
.0027	70.9562	1.8491
.0029	66.8796	1.7631
.0031	62.6102	1.7292
.0033	55.8396	1.6319
.0035	53.6582	1.5991
.0037	50.2661	1.5476
.0038	49.5911	1.5372
.0040	49.8752	1.5418
.0042	46.4592	1.4883
.0044	46.4100	1.4877
.0046	43.2499	1.4364
.0048	43.5280	1.4413
.0050	43.4409	1.4400
.0052	41.9629	1.4155
.0053	39.0955	1.3665
.0055	39.2053	1.3686
.0057	38.7625	1.3610
.0059	38.4350	1.3554
.0061	38.1552	1.3501
.0063	37.8437	1.3452
.0065	37.3620	1.3367
.0067	35.4850	1.3028
.0068	36.2256	1.3164
.0070	35.2263	1.2982
.0072	36.2327	1.3167
.0074	35.8390	1.3096
.0076	36.8292	1.3277
.0078	32.5363	1.2480
.0080	32.6178	1.2496
.0082	31.1469	1.2212
.0084	35.0416	1.2954
.0085	34.2589	1.2809
.0087	33.2455	1.2619
.0093	31.8565	.5511
.0102	32.3613	.5542
.0113	30.9784	.4944
.0124	30.6988	.4921
.0135	29.0370	.4788
.0147	28.3699	.4384
.0160	27.7982	.4342
.0174	27.4045	.4313
.0187	25.3456	.4149
.0201	25.6770	.3908
.0216	25.9038	.3926
.0231	25.6963	.3911
.0247	24.4974	.3600
.0264	24.5194	.3602
.0281	23.9449	.3558
.0298	24.0044	.3378
.0317	22.9467	.3301
.0336	22.6492	.3277
.0356	22.2904	.3096
.0376	21.4245	.3032
.0390	21.7769	.5063

TABLE PI-H -280 GEV

T	SIGMA MB/(GEV**2)	ERROR
.0022	91.1656	1.9634
.0023	80.5810	1.8278
.0025	74.7674	1.7508
.0027	71.2231	1.7041
.0029	66.4504	1.6437
.0031	57.7050	1.5305
.0033	57.5620	1.5276
.0035	57.0492	1.5209
.0037	53.1290	1.4680
.0038	50.0974	1.4259
.0040	49.3722	1.4159
.0042	48.7017	1.4067
.0044	47.4766	1.3892
.0046	43.4262	1.3290
.0048	44.3803	1.3438
.0050	41.5905	1.3011
.0052	42.7497	1.3194
.0053	41.3864	1.2984
.0055	40.5645	1.2856
.0057	39.7321	1.2725
.0059	39.3237	1.2661
.0061	38.1235	1.2468
.0063	38.0625	1.2459
.0065	38.1244	1.2471
.0067	37.9007	1.2435
.0068	36.8934	1.2270
.0070	36.2614	1.2165
.0072	36.3376	1.2179
.0074	35.3279	1.2009
.0076	36.7620	1.2251
.0078	34.7701	1.1915
.0080	32.3834	1.1500
.0082	34.2985	1.1835
.0084	33.6199	1.1718
.0085	33.2605	1.1656
.0087	32.6671	1.1552
.0089	33.0310	1.1592
.0091	33.4462	1.1658
.0093	34.4983	1.1831
.0099	31.9039	.5081
.0108	30.8753	.4988
.0118	29.8033	.4470
.0129	29.0698	.4416
.0141	28.5554	.4378
.0153	28.6598	.4062
.0166	28.3419	.4041
.0179	27.6326	.3992
.0193	27.2293	.3707
.0208	26.4250	.3653
.0223	25.9218	.3618
.0238	25.6089	.3596
.0254	24.9482	.3345
.0271	24.5205	.3315
.0288	24.4045	.3306
.0306	23.4343	.3071
.0325	23.0194	.3040
.0343	21.7335	.2950
.0363	22.2719	.2844
.0384	21.1228	.2764

TABLE PI-H -300 GEV

TABLE 5 (cont'd)

T	SIGMA MB/(GEV**2)	ERROR
.0022	92.8086	2.1210
.0023	82.9532	1.9934
.0025	76.8804	1.9137
.0027	70.2504	1.8263
.0029	64.6308	1.7504
.0031	62.3617	1.7181
.0033	53.5573	1.5924
.0035	54.3211	1.6041
.0037	53.6285	1.5942
.0038	54.0034	1.6002
.0040	50.6307	1.5498
.0042	47.1364	1.4958
.0044	45.0607	1.4628
.0046	43.3818	1.4356
.0048	43.8572	1.4438
.0050	42.6393	1.4239
.0052	40.1660	1.3823
.0053	42.6090	1.4239
.0055	41.1381	1.3994
.0057	41.4033	1.4041
.0059	37.5867	1.3380
.0061	38.5324	1.3550
.0063	38.8099	1.3600
.0065	37.0125	1.3283
.0067	34.8729	1.2895
.0068	35.5264	1.3017
.0070	35.2175	1.2961
.0072	33.9927	1.2735
.0074	36.1348	1.3131
.0076	34.9348	1.2913
.0078	32.3827	1.2433
.0080	30.2971	1.2027
.0082	32.1404	1.2388
.0084	37.0007	1.3293
.0085	34.9677	1.2923
.0087	31.9222	1.2349
.0093	32.5105	.5562
.0103	31.6737	.5004
.0114	29.2219	.4803
.0126	30.6951	.4923
.0138	28.8727	.4423
.0151	28.0614	.4362
.0164	28.0100	.4360
.0178	27.0560	.4010
.0193	27.1752	.4019
.0208	26.5598	.3974
.0224	25.8977	.3700
.0241	25.1014	.3642
.0258	24.5993	.3604
.0276	24.4315	.3406
.0295	23.5197	.3339
.0313	23.0421	.3302
.0333	22.4007	.3100
.0354	22.3428	.3091
.0374	21.6184	.3035
.0389	21.0300	.4433

TABLE PI-H -325 GEV

T	SIGMA MB/(GEV**2)	ERROR
.0022	95.7871	2.3406
.0023	82.5149	2.1633
.0025	74.8951	2.0579
.0027	69.9022	1.9866
.0029	64.2836	1.9049
.0031	57.4068	1.8003
.0033	56.9245	1.7924
.0035	55.5782	1.7718
.0037	48.8127	1.6611
.0038	52.3159	1.7204
.0040	51.4172	1.7061
.0042	45.7689	1.6102
.0044	46.9593	1.6315
.0046	45.8480	1.6125
.0048	41.9098	1.5420
.0050	43.8813	1.5782
.0052	41.1437	1.5285
.0053	39.4449	1.4969
.0055	41.2137	1.5303
.0057	41.6254	1.5382
.0059	36.1942	1.4345
.0061	38.5194	1.4800
.0063	34.9327	1.4096
.0065	37.8066	1.4666
.0067	34.8595	1.4084
.0068	34.3487	1.3981
.0070	35.8747	1.4290
.0072	37.3219	1.4576
.0074	34.7939	1.4074
.0076	33.7441	1.3861
.0078	36.3880	1.4395
.0080	32.7352	1.3654
.0082	36.4867	1.4416
.0084	35.4865	1.4217
.0085	34.2449	1.3967
.0087	35.7181	1.4265
.0089	34.3035	1.3974
.0091	33.4566	1.3800
.0093	33.8602	1.3882
.0099	32.7860	.5576
.0111	31.1573	.5433
.0123	31.3618	.5047
.0136	29.1644	.4867
.0149	28.7460	.4832
.0163	27.7785	.4444
.0178	27.2613	.4402
.0193	26.4184	.4334
.0209	26.4506	.4089
.0226	26.2948	.4076
.0244	24.9688	.3768
.0263	24.5678	.3737
.0281	24.5249	.3734
.0301	23.7518	.3502
.0322	23.1911	.3460
.0342	22.7947	.3429
.0364	21.7042	.3202
.0385	21.7195	.3507

TABLE PI-H -345 GEV

TABLE 5 (cont'd)

T	SIGMA MB/(GEV**2)	ERROR
.0022	136.7833	4.6984
.0023	126.7451	4.4630
.0025	124.0149	4.3792
.0027	117.8995	4.2489
.0029	112.2116	4.1328
.0031	108.8314	4.0628
.0033	97.4670	3.8407
.0035	98.2173	3.8530
.0037	89.3651	3.6740
.0038	88.6235	3.6580
.0040	90.2484	3.6909
.0042	95.2520	3.7917
.0044	91.2985	3.7120
.0046	80.6547	3.4889
.0048	97.5825	3.8375
.0050	85.7269	3.5968
.0052	83.9965	3.5603
.0053	84.0573	3.5615
.0055	87.2575	3.6286
.0057	81.4163	3.5050
.0059	82.0521	3.5185
.0061	82.8118	3.5347
.0063	84.6086	3.5727
.0065	78.5364	3.4420
.0067	79.4471	3.4618
.0068	77.9901	3.4300
.0070	78.1353	3.4330
.0072	77.4427	3.4176
.0074	70.2744	3.2556
.0076	78.5048	3.4409
.0078	74.7203	3.3568
.0080	76.9154	3.4057
.0082	73.9801	3.3401
.0084	72.4268	3.3048
.0085	69.6970	3.2419
.0087	79.3078	3.4582
.0091	76.5658	1.9590
.0097	75.6752	1.9439
.0102	72.4480	1.8989
.0108	72.8291	1.9027
.0114	70.2455	1.8687
.0119	68.1988	1.8418
.0125	69.4131	1.8587
.0130	63.8995	1.7839
.0136	63.4530	1.7781
.0143	65.2622	1.5622
.0150	66.0564	1.5722
.0158	63.5616	1.5427
.0165	65.1532	1.5624
.0173	60.3446	1.5040
.0180	64.1399	1.5508
.0188	62.4855	1.5310
.0195	61.0120	1.5130
.0203	60.5647	1.5075
.0210	58.6581	1.4837
.0218	60.5270	1.5071
.0226	57.2682	1.3111
.0236	59.1167	1.3319
.0245	57.1577	1.3094
.0254	56.7809	1.3047
.0264	57.1124	1.3080
.0273	54.7953	1.2807
.0282	56.7934	1.3032
.0292	56.6773	1.3011
.0301	52.6105	1.2527
.0311	54.5590	1.2748
.0321	52.8699	1.1445
.0332	53.5332	1.1505
.0343	50.6463	1.1177
.0355	51.4224	1.1248
.0366	48.4377	1.0902
.0377	48.1716	1.0855
.0388	47.8305	1.0800

TABLE P-H 100 GEV

T	SIGMA MB/(GEV**2)	ERROR
.0022	131.3619	3.7159
.0023	124.6563	3.5960
.0025	111.5033	3.3895
.0027	109.5665	3.3543
.0029	106.7000	3.3077
.0031	105.2449	3.2842
.0033	102.6738	3.2438
.0035	94.1929	3.1072
.0037	96.5972	3.1470
.0038	85.6162	2.9632
.0040	92.0566	3.0730
.0042	90.6839	3.0503
.0044	87.1288	2.9901
.0046	90.6938	3.0508
.0048	84.6734	2.9480
.0050	83.0198	2.9191
.0052	91.9701	3.0725
.0053	86.3882	2.9779
.0055	81.0501	2.8844
.0057	82.8315	2.9160
.0059	79.2290	2.8519
.0061	77.8079	2.8262
.0063	76.8803	2.8094
.0065	81.6026	2.8944
.0067	76.8280	2.8085
.0068	79.1565	2.0508
.0070	75.9279	2.7921
.0072	70.3327	2.6873
.0074	76.5667	2.8040
.0076	74.4712	2.7654
.0078	73.2748	2.7432
.0080	71.4083	2.7082
.0082	71.3950	2.7080
.0084	69.0867	2.6640
.0085	75.4866	2.7849
.0087	73.6664	2.7512
.0091	75.8272	1.6100
.0097	73.5173	1.5831
.0102	73.3269	1.5791
.0109	70.5855	1.3409
.0116	69.4343	1.3302
.0124	70.7043	1.3429
.0131	69.4634	1.3317
.0139	67.2418	1.3108
.0146	66.3873	1.3030
.0154	67.1643	1.3111
.0162	67.0284	1.1720
.0172	65.4431	1.1585
.0181	63.5217	1.1418
.0190	63.2115	1.1393
.0200	61.8903	1.1276
.0209	61.9041	1.1280
.0219	61.8340	1.1275
.0228	57.6550	1.0888
.0238	59.4038	1.0088
.0250	56.6395	.9850
.0261	59.2203	1.0070
.0272	57.6717	.9935
.0283	55.8972	.9777
.0295	53.5735	.9567
.0306	53.1929	.9528
.0318	52.8257	.8784
.0331	52.4216	.8743
.0344	51.4383	.8652
.0357	50.1993	.8537
.0371	49.2297	.8444
.0384	48.5186	.8371
.0392	49.3270	1.5776

TABLE P-H 150 GEV

TABLE 5 (cont'd)

T	SIGMA MB/(GEV**2)	ERROR
.0022	134.2575	3.9604
.0023	126.9640	3.8118
.0025	121.4021	3.7043
.0027	114.4817	3.5837
.0029	103.6448	3.4038
.0031	97.1731	3.2928
.0033	100.1123	3.3409
.0035	101.3265	3.3608
.0037	95.4665	3.2623
.0038	97.1020	3.2906
.0040	89.4887	3.1594
.0042	90.9624	3.1858
.0044	87.0266	3.1166
.0046	86.6141	3.1096
.0048	92.1241	3.2074
.0050	87.2862	3.1223
.0052	86.6757	3.1116
.0053	81.6564	3.0203
.0055	78.6301	2.9639
.0057	80.0676	2.9910
.0059	86.4310	3.1076
.0061	77.8662	2.9497
.0063	78.5569	2.9627
.0065	82.6683	3.0393
.0067	80.4138	2.9975
.0068	82.3138	3.0327
.0070	74.9717	2.8943
.0072	77.8097	2.9489
.0074	82.0498	3.0278
.0076	73.7642	2.8708
.0078	77.3411	2.9396
.0080	72.9449	2.8548
.0082	77.2064	2.9370
.0084	73.5291	2.8662
.0085	78.2504	2.9568
.0087	71.7712	2.8318
.0089	76.1042	2.9105
.0091	78.9399	2.9637
.0093	75.0997	2.8893
.0098	73.0006	1.4222
.0105	71.0325	1.4004
.0114	70.4106	1.2460
.0123	71.2103	1.2531
.0132	67.7567	1.2228
.0142	67.5339	1.2212
.0151	67.6464	1.2227
.0161	66.5324	1.2073
.0173	64.9386	1.0944
.0184	64.1758	1.0883
.0195	62.9163	1.0778
.0206	61.6556	1.0672
.0219	60.0805	.9755
.0232	59.8126	.9734
.0245	60.1470	.9761
.0258	58.0272	.9587
.0271	57.2376	.9519
.0285	56.1692	.8818
.0300	55.1983	.8738
.0315	54.1083	.8647
.0330	53.2586	.8573
.0345	52.6403	.8516
.0361	50.5620	.7861
.0378	49.9912	.7807
.0390	50.3191	1.1737

TABLE P-H 250 GEV

T	SIGMA MB/(GEV**2)	ERROR
.0022	137.1950	4.7741
.0023	125.1295	4.5214
.0025	117.8490	4.3681
.0027	118.3003	4.3664
.0029	98.9008	3.9885
.0031	103.3411	4.0747
.0033	101.2918	4.0350
.0035	102.1058	4.0528
.0037	89.4786	3.7957
.0038	94.9263	3.9114
.0040	87.9107	3.7658
.0042	88.7573	3.7855
.0044	87.5808	3.7617
.0046	87.0326	3.7511
.0048	88.3173	3.7798
.0050	85.1282	3.7119
.0052	93.8706	3.8986
.0053	87.2817	3.7600
.0055	85.6914	3.7262
.0057	77.4567	3.5431
.0059	84.7445	3.7064
.0061	83.8545	3.6873
.0063	75.9982	3.5106
.0065	76.9852	3.5791
.0067	78.5758	3.5701
.0068	72.1824	3.4219
.0070	74.7595	3.4826
.0072	81.4779	3.6359
.0074	79.1866	3.5845
.0076	78.8565	3.5772
.0078	73.3810	3.4508
.0080	75.4525	3.4993
.0082	70.4425	3.3812
.0084	75.5914	3.5027
.0085	79.3933	3.5898
.0087	74.1766	3.4700
.0089	76.6831	3.5193
.0091	72.7495	3.4263
.0093	77.2956	3.5271
.0099	71.2525	1.5120
.0108	72.7505	1.5245
.0118	70.3511	1.3676
.0129	70.6681	1.3712
.0141	68.0661	1.3465
.0153	66.6433	1.3130
.0164	65.5502	1.2248
.0177	64.2096	1.2129
.0190	64.4803	1.2160
.0205	61.2191	1.1087
.0220	61.1703	1.1085
.0235	58.2725	1.0819
.0250	60.3356	1.1008
.0266	57.4699	1.0125
.0282	58.8991	1.0246
.0299	54.6410	.9861
.0317	55.8258	.9446
.0336	52.3309	.9133
.0355	51.7819	.9071
.0373	48.9129	.8799
.0388	49.6545	1.1426

TABLE P-H 300 GEV

TABLE 6

Values of ρ and b resulting from the fits

P_o GeV/c	t-region $(GeV/c)^2$	No of events	$\rho \pm \Delta\rho$	$b \pm \Delta b$ $(GeV/c)^{-2}$
		π^-p-scattering (WA9)		
30	.002-.02	20,000	- .04±.02	-
50	.002-.04	78,000	-.003±.013	10.1±.3
80	"	94,000	+.017±.013	10.7±.3
100	"	98,000	+.023±.013	10.8±.3
120	"	68,000	+.052±.013	10.8±.3
140	.002-.03	19,000	+ .03±.02	10.4±.8
		π^-p-scattering (NA8)		
100	.002-.04	100,000	.048±.012	10.5±.3
150	"	130,000	.048±.012	10.1±.3
200	"	140,000	.064±.011	10.3±.3
250	"	80,000	.078±.013	10.4±.3
280	"	115,000	.087±.012	10.5±.3
300	"	150,000	.090±.012	10.7±.3
325	"	120,000	.084±.012	10.9±.3
345	"	110,000	.075±.012	11.0±.3
		pp-scattering (NA8)		
100	.002-.04	85,000	-.092±.014	12.0±.3
150	"	130,000	-.040±.014	12.1±.3
250	"	120,000	-.041±.014	12.2±.3
300	"	80,000	-.028±.016	12.4±.3

TABLE 7

Values of the constants b_o, b_1 and b_2 obtained by fitting the existing data on the slope parameter b with the formula $b=b_o+b_1(p/p_o)^{-q}+b_2 \ln(p/p_o)$ with p_o=1 GeV/c. b_1 was allowed to be different for particle and antiparticle, respectively. b_1^+ stands for the value found for positively charged particles and b_1^- for negatively charged particles. NDF is the number of degrees of freedom in the fits.

$\|t\|$, $(GeV/c)^2$	particle	b_o $(GeV/c)^{-2}$	b_1^+ $(GeV/c)^{-2}$	b_1^- $(GeV/c)^{-2}$	b_2 $(GeV/c)^{-2}$	q	χ^2/NDF
.02	p	11.13±.22	-6.21±.53	-	.30±.04	.5(fix)	82/69
.02	π^-	9.11±.17	-	.65(fix)	.29±.08	.5(fix)	17/22
.2	p/p^-	9.26±.29	-4.94±.52	7.23±.59	.28±.05	.5(fix)	32/59
.2	K^+/K^-	6.77±.33	-5.72±.51	1.01±.54	.24±.06	.5(fix)	41/44
.2	π^+/π^-	6.95±.28	- .73±.45	.65±.45	.27±.05	.5(fix)	53/60
.2	p/p^-	9.25±.29	-5.05±.55	7.49±.74	.28±.05	.52±.02	31/59
.2	K^+/K^-	6.55±.30	-5.98±.50	1.60±.57	.27±.06	.56±.03	37/44
.4	p	9.67±.47	-7.51±.80	-	.10±.08	.5(fix)	41/29
.4	π^-	6.13±.11	-	.65(fix)	.25±.07	.5(fix)	33/24

Table 8

Values of the constants b_0, c and d, obtained by fitting the data on pp and πp scattering at 200 GeV of ref. [50], on πp scattering at 8 and 16 GeV/c of ref. [42] and our data at 200 GeV with the following parameterization: $b|t| = b_0 - 2c|t| + 3d|t|^2$.

Particles	p_o GeV/c	b_o $(GeV/c)^{-2}$	c $(GeV/c)^{-4}$	d $(GeV/c)^{-6}$
pp	200	12.47 ± 0.10	6.83 ± 0.50	4.94 ± 0.7
πp	200	10.73 ± 0.20	7.25 ± 0.90	4.5 ± 1.2
πp	8 ÷ 16	10.18 ± 0.12	7.76 ± 0.60	5.3 ± 0.7

FIGURE CAPTIONS

Fig. 1 Lay-out of the experiment: B1-B8 are bending magnets; CED1, CED2 are differential Cerenkov counters; TH1, TH2 are threshold Cerenkov counters; BS1-BS4 are multiwire proportional chambers of the beam spectrometer; PC1-PC6 are blocks of multiwire proportional chambers; S1-S2, A1-A3 are scintillator counters; and IKAR is the recoil detector. In the beam lay-out all quadrupoles and correction dipoles and all collimators except the momentum defining slit have been omitted.

Fig. 2 Particle spectrum at 150 GeV/c determined by scanning the pressure in one of the CEDARs.

Fig. 3 A schematic view of two cells of the recoil detector IKAR.

Fig. 4 Time diagram of pulses produced in IKAR by a recoil particle.

Fig. 5 The energies T_A, T_B, T_{AB}, deposited on the IKAR electrodes A,B, and A + B as functions of the recoil energy T_r. The calculation was done using the energy-range curve for protons in hydrogen at 10 atm pressure.

Fig. 6 Correlation between the recoil energy T_r^* and the energy T_{AB} deposited in IKAR for a sample of events before χ^2 cut. The spot size is proportional to the number of events. T_r^* was calculated from the scattering angle of the forward particle θ assuming elastic scattering: $T_r^* = (p^*\theta)^2/2M_p$ where p^* is the mean absolute momentum of the beam particles and M_p is the proton mass.

Fig. 7 Same as in fig. 6 but for events left after the χ^2 cut.

Fig. 8 Correlation between the recoil energy T_r^* and the delay time t_K of the cathode signal with respect to the passage of the beam particle for a sample of events after the χ^2 cut. This correlation was not used for selection of the elastic events.

FIGURE CAPTIONS (Cont'd)

Fig. 9 Correlation between the recoil energy T_r^* and the difference in the delay times t_A and t_B for a sample of events after the χ^2 cut. The elastic scattering kinematic requires $|t_A - t_B| \sim \sqrt{T_r^*}$. This correlation was not used in selection of the elastic events.

Fig. 10 Momentum distribution of elastically scattered pions. The right-side tail in this distribution is due to bremstrahlung effect.

Fig. 11 Correction to the α-source calibration of the recoil energy scale. T_r is the recoil energy calculated from the V_{AB} amplitude. T_r^* is the recoil energy calculated from the scattering angle of the forward particle. The straight line in the figure is the result of the fit $F_1(T_r^*) = a_0 + a_1 T_r^*$ with $a_0 = (-45 \pm 5)$ KeV, $a_1 = 0.020 \pm 0.002$.

Fig. 12 Distribution of the delay times t_A used to determine the effective target length. The bin width of the distribution is 50 ns. $(t_A)_G$ and $(t_A)_K$ indicate the delay times corresponding to the tracks lying in the planes of the grid and the cathode, respectively.

Fig. 13 The upper part of the figure shows the χ^2 distribution for a sample of events in a T_r bin. The dashed line represents the χ^2 distribution of the test events normalized to the number of the physical events. The relative amount of the test events beyond $\chi^2_{cut} = 15$ gives the number of good events rejected by the χ^2 cut (1.5%). The lower part of the figure shows the difference between the physical and the test events distributions used to find the background under the χ^2 peak (1.4%).

FIGURE CAPTIONS (cont'd)

Fig. 14 Corrections that were applied to the measured differential cross-sections for the first class of events (a) and for the second class of events (b):

1. the loss of good events caused by the χ^2 cut;
2. the level of background;
3. the cathode inefficiency;
4. the radiative correction;
5. the total correction.

Fig. 15 Examples of the fits by the interference formulae (20) to the measured differential cross-sections.
a) pp-scattering and b) π^-p-scattering at 250 GeV/c.

Fig. 16 a) The values of $I^-(E)$ obtained from $d\sigma/dt$ (t=0) for π^-p charge exchange reaction [23].
The solid line is the result of calculation [22] of the integral $I^-(E)$ using eq. (23).
b) Experimental data on $\sigma^-_{\pi p} = (\sigma_{\pi^-p} - \sigma_{\pi^+p})/2$ from ref. [21].
The curve represents the parametrization HK-80/2[22]:
$\sigma^-_{\pi p} = 2.93(p/p_o)^{-0.47}$ mb, $p_o = 1$ GeV/c.

Fig. 17 Experimental results on $\rho_{\pi^-p}(E,t=0)$ in the momentum range $10 < p < 120$ GeV/c.
a) The data from the measurements previous to our experiment and b) present situation.
The curve in the figures are the prediction of the dispersion relation calculation (HK-80/2 [22]).

Fig. 18 Experimental data on $\rho_{pp}(E,t=0)$.
The full line is the result of a dispersion relation calculation by Grein [28].
The dashed area corresponds to the uncertainty estimated in ref.[28].

FIGURE CAPTIONS (Cont'd)

Fig. 19 Experimental data on $\sigma_{\pi^{\pm}p}(E)$.
The dash-dotted line represents the parametrization suggested by Höhler et al., [22] (HK-80/2).
The full line is a result of a simultaneous fit to the data on σ_{tot} and ρ_{π^-p}.
The cross hatched area corresponds to one standard deviation of the parameter E_{break}.

Fig. 20 Experimental data on $\rho_{\pi^-p}(E,t=0)$.
The dash-dotted line is the result of a dispersion relation calculation with parametrization for $\sigma^+_{\pi p}$ (E) suggested by Höhler et al. [22] (HK-80/2).
The dotted line is the result of a simultaneous fit to the σ_{tot} and ρ data.
The full line is the result of a dispersion relation calculation with the parametrization for $\sigma^+_{\pi p}$ (E) obtained from the simultaneous fit and with assuming a break at 4000 GeV.

Fig. 21 Slope parameters b at different t-value as functions of the incident energy for π^-p and pp-scattering. The points at $|t| = 0.2$ (GeV/c)^2 and $|t| = 0.4$ (GeV/c)^2 are from our compilation [16] of the world data.
The solid lines represent the results of the fits to the data with parametrization (42). The parameters found from the fits are given in table 7.

Fig. 22 Our compilation of the world data on the slope parameters at $-t = 0.2$ (GeV/c)^2 for $p^{\pm}p$, $K^{\pm}p$ and $\pi^{\pm}p$ scattering.
The solid lines show the slopes calculated using eq. (42) with parameters b_o, b_1 and b_2 listed in table 7, and $q = 0.5$.
The dashed lines represent only a linear part of eq. (42).

Fig. 23 t-dependence of hadronic slopes for pp elastic scattering at 200 GeV and π^-p elastic scattering at 8÷16 GeV and 200 GeV.
The solid lines represent the results of the fits to the data using the parametrization: $b(t) = b_o - 2c|t| + 3d|t|^2$. The dashed lines shows b(t) as obtained in ref. [50] using the A.Q.M. parametrization.

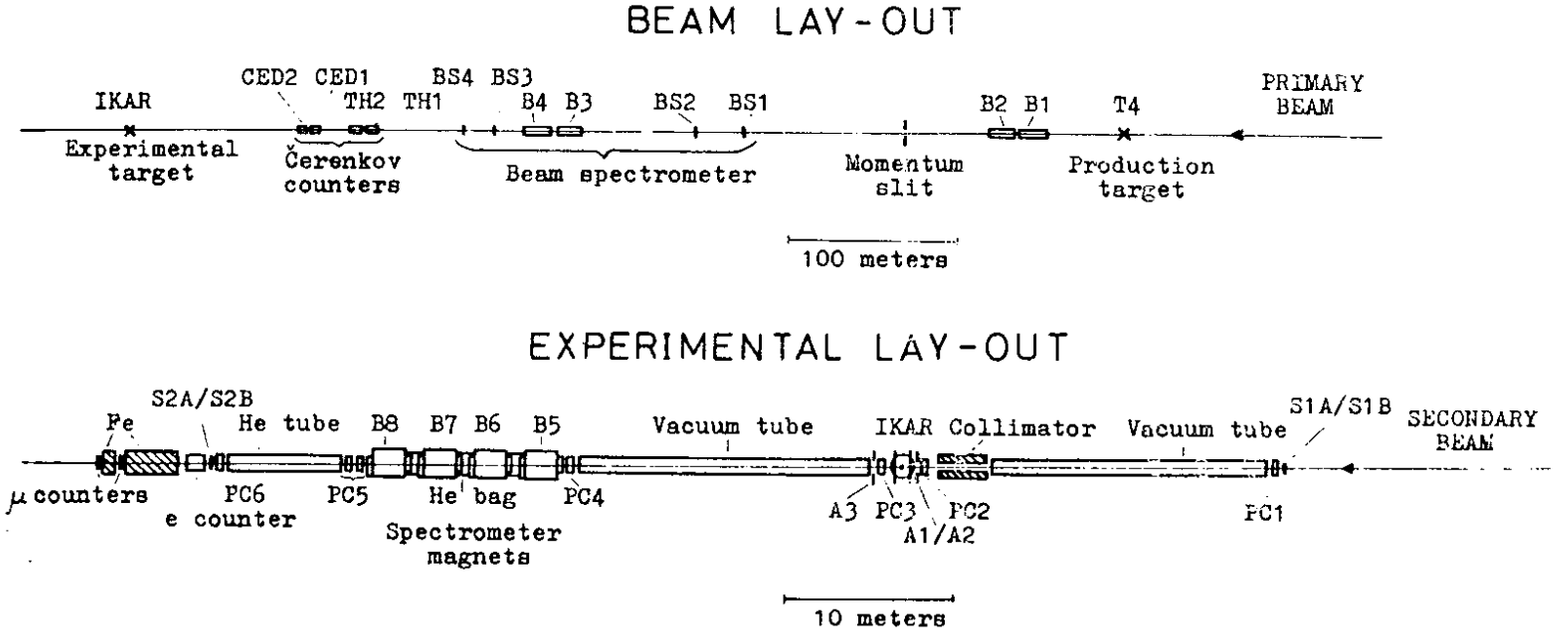
BEAM LAY-OUT
IKAR
CED2 CED1
TH2 TH1
BS4 BS3
B4 B3
BS2 BS1
B2 B1
T4
PRIMARY BEAM
Experimental target
Čerenkov counters
Beam spectrometer
Momentum slit
Production target
100 meters
EXPERIMENTAL LAY-OUT
S2A/S2B
Fe
He tube
B8 B7 B6 B5
Vacuum tube
IKAR Collimator
Vacuum tube
S1A/S1B
SECONDARY BEAM
μ counters
PC6
e counter
PC5
He bag
PC4
Spectrometer magnets
A3 PC3 PC2
A1/A2
PC1
10 meters

Fig. 1

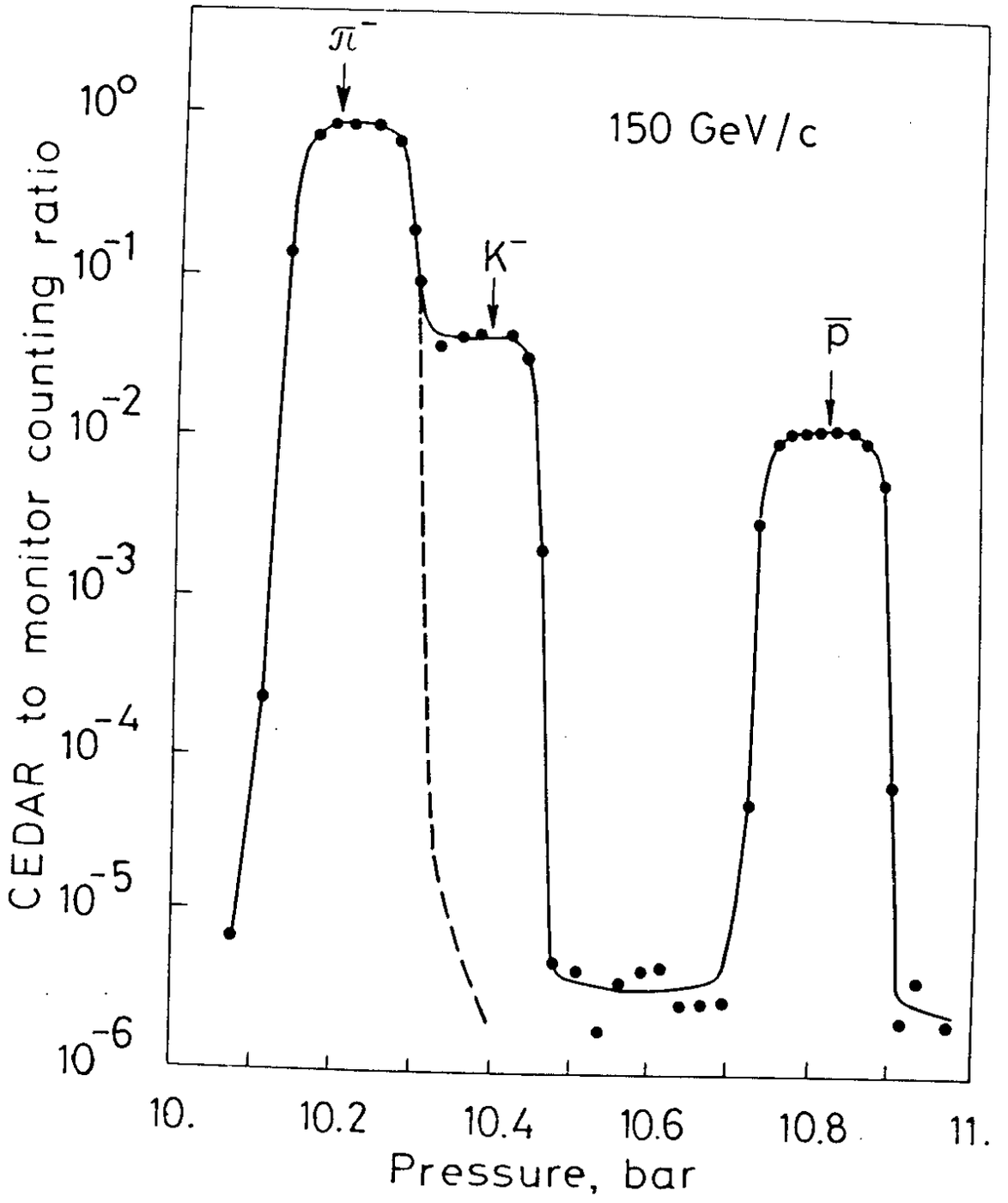
π^-
150 GeV/c
K^-
$\bar{p}$
CEDAR to monitor counting ratio
10^{0}
10^{-1}
10^{-2}
10^{-3}
10^{-4}
10^{-5}
10^{-6}
10.
10.2
10.4
10.6
10.8
11.
Pressure, bar

Fig. 2

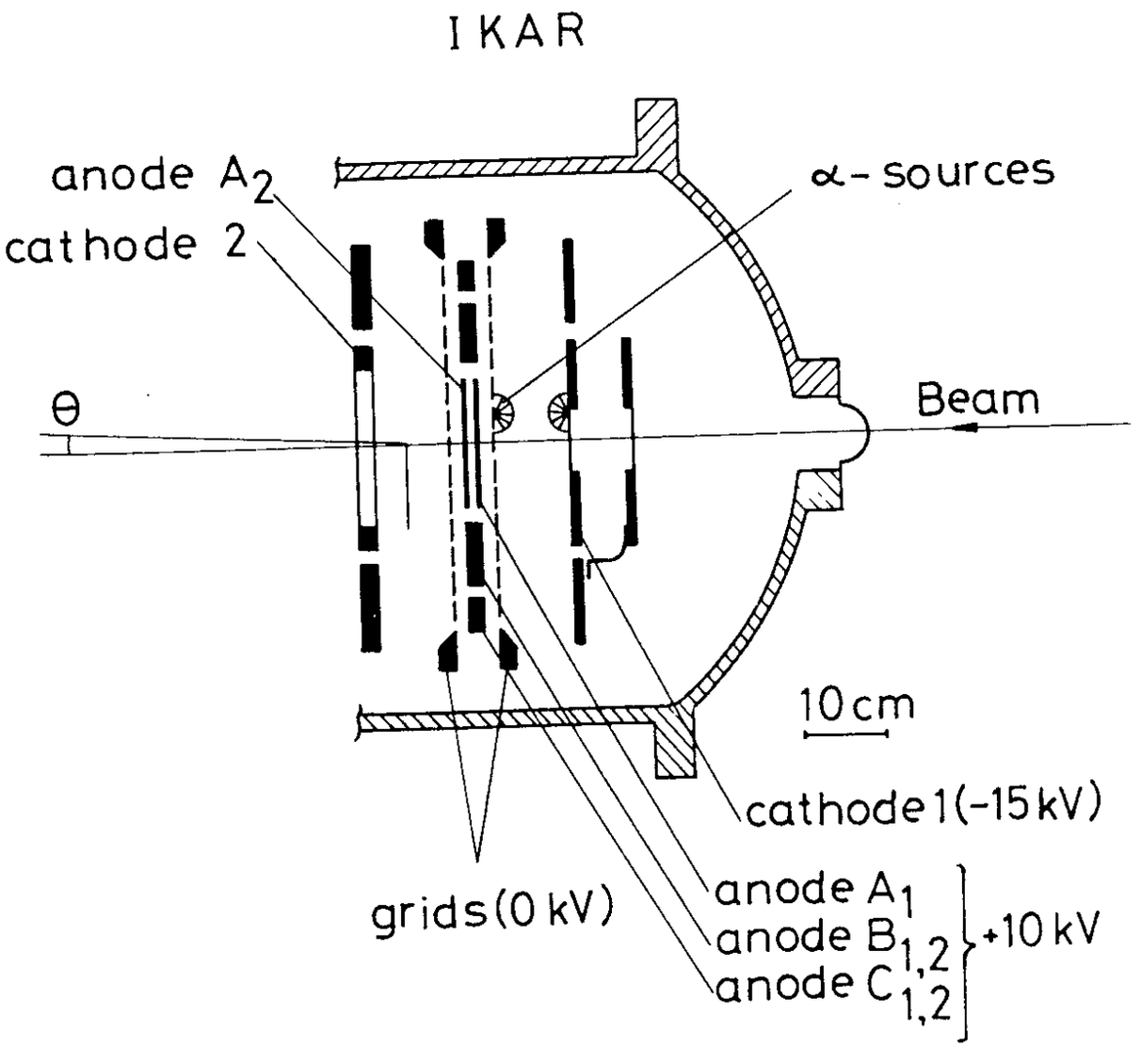
IKAR
anode A_2
cathode 2
α - sources
Θ
Beam
10 cm
cathode 1 (-15 kV)
grids (0 kV)
anode A_1
anode $B_{1,2}$
anode $C_{1,2}$
+10 kV

Fig. 3

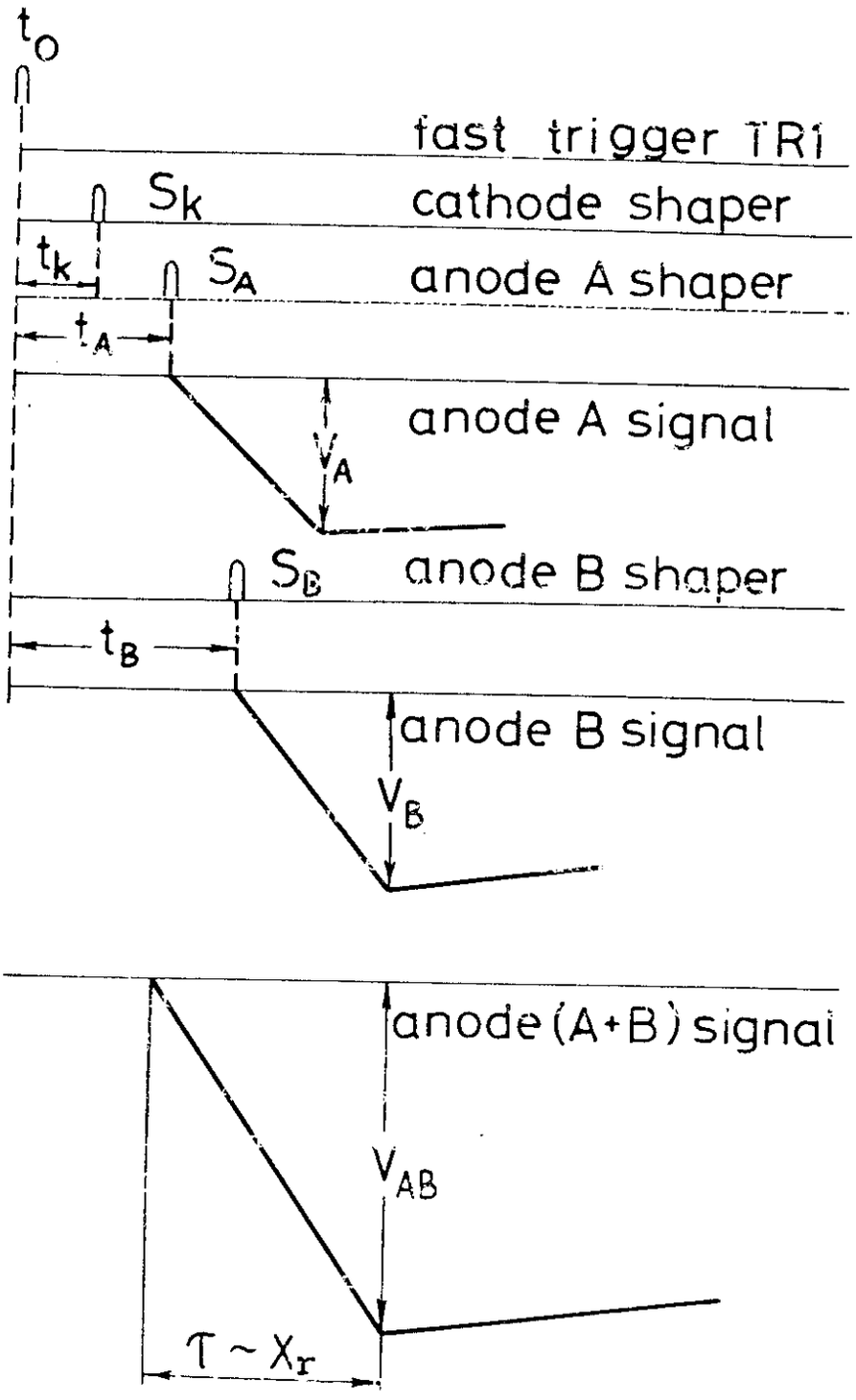
t_o
fast trigger TR1
S_k
cathode shaper
t_k
S_A
anode A shaper
t_A
anode A signal
V_A
S_B
anode B shaper
t_B
anode B signal
V_B
anode (A+B) signal
V_{AB}
$T \sim X_r$

Fig. 4

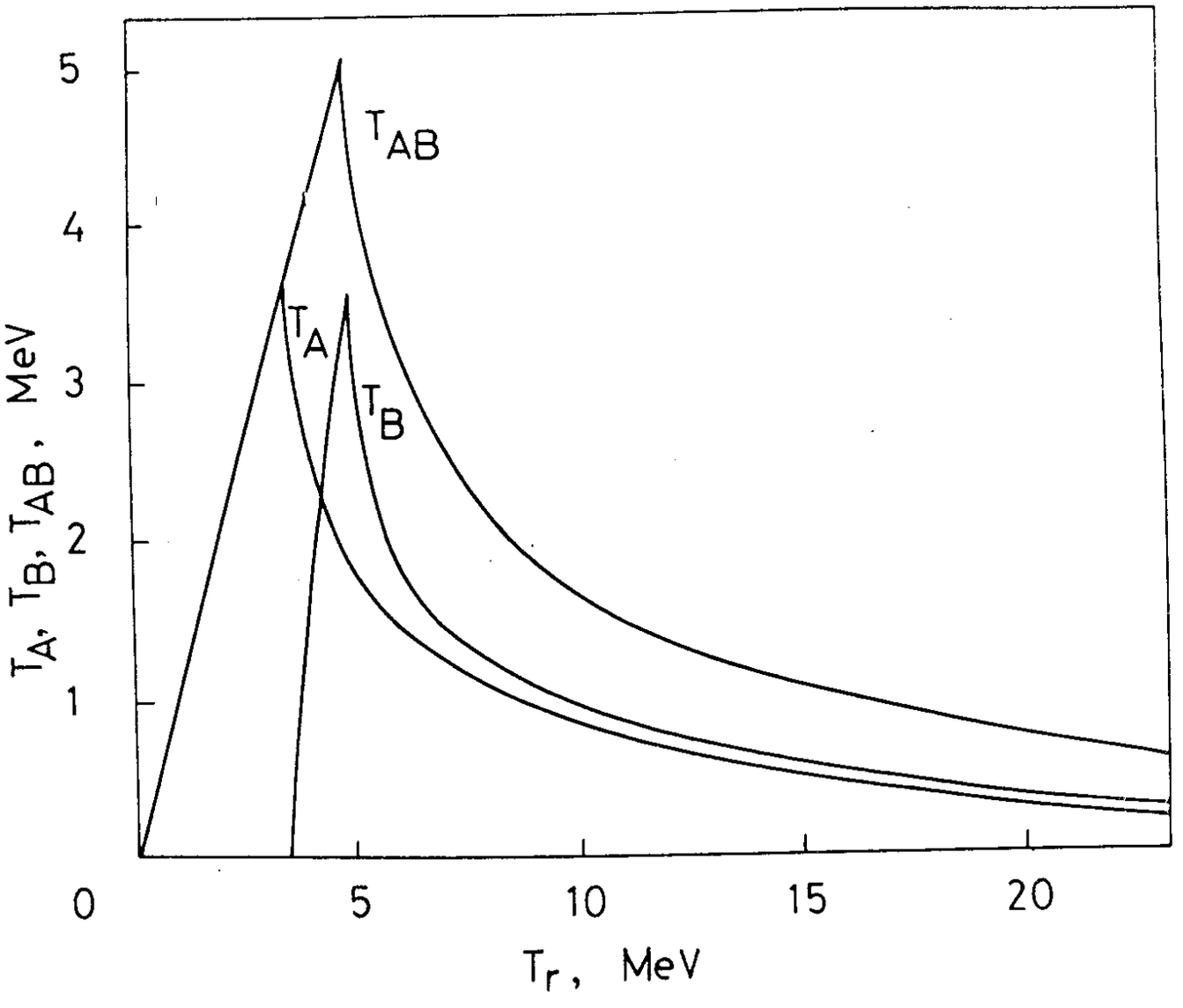

Fig. 5

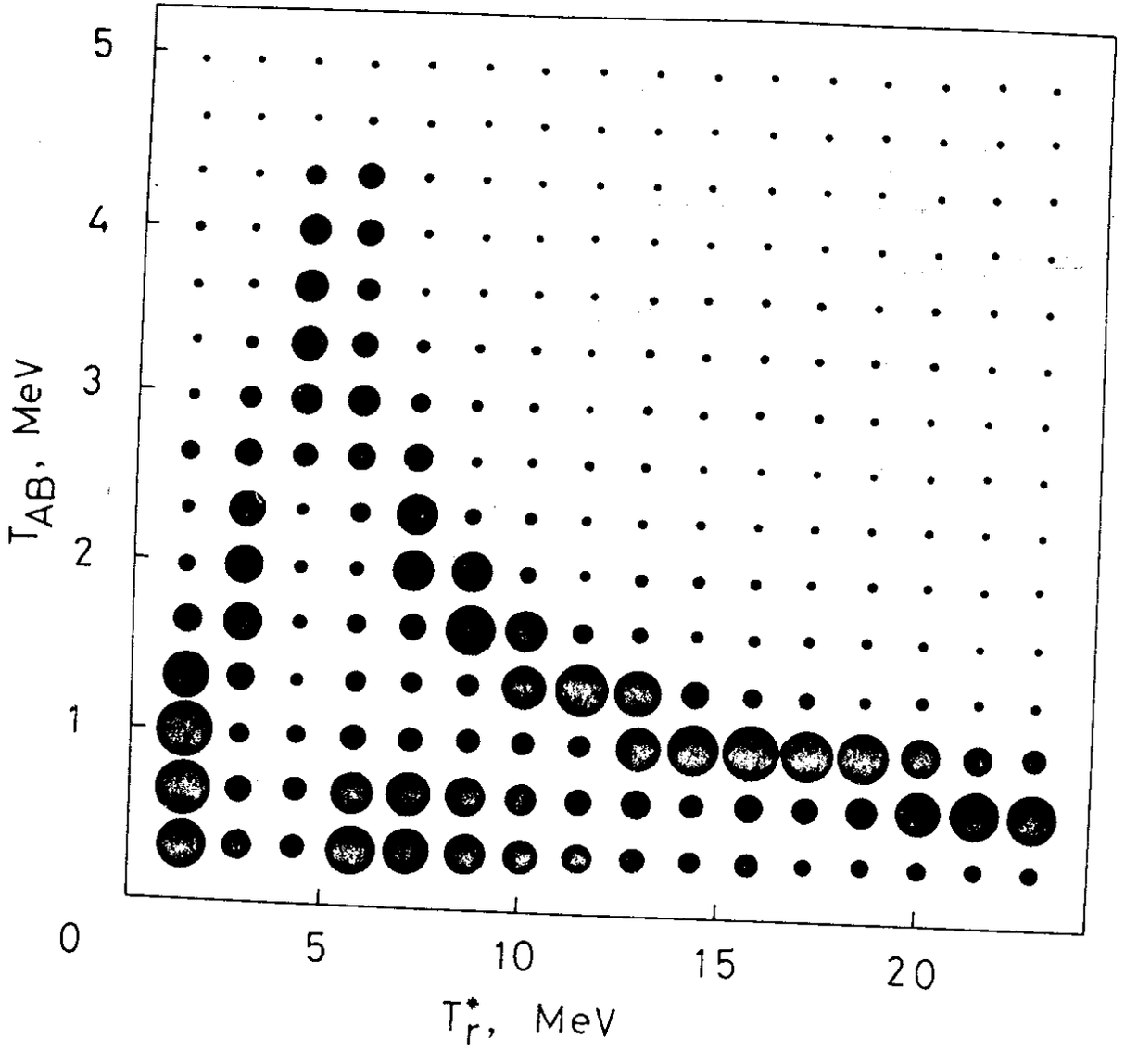

Fig. 6

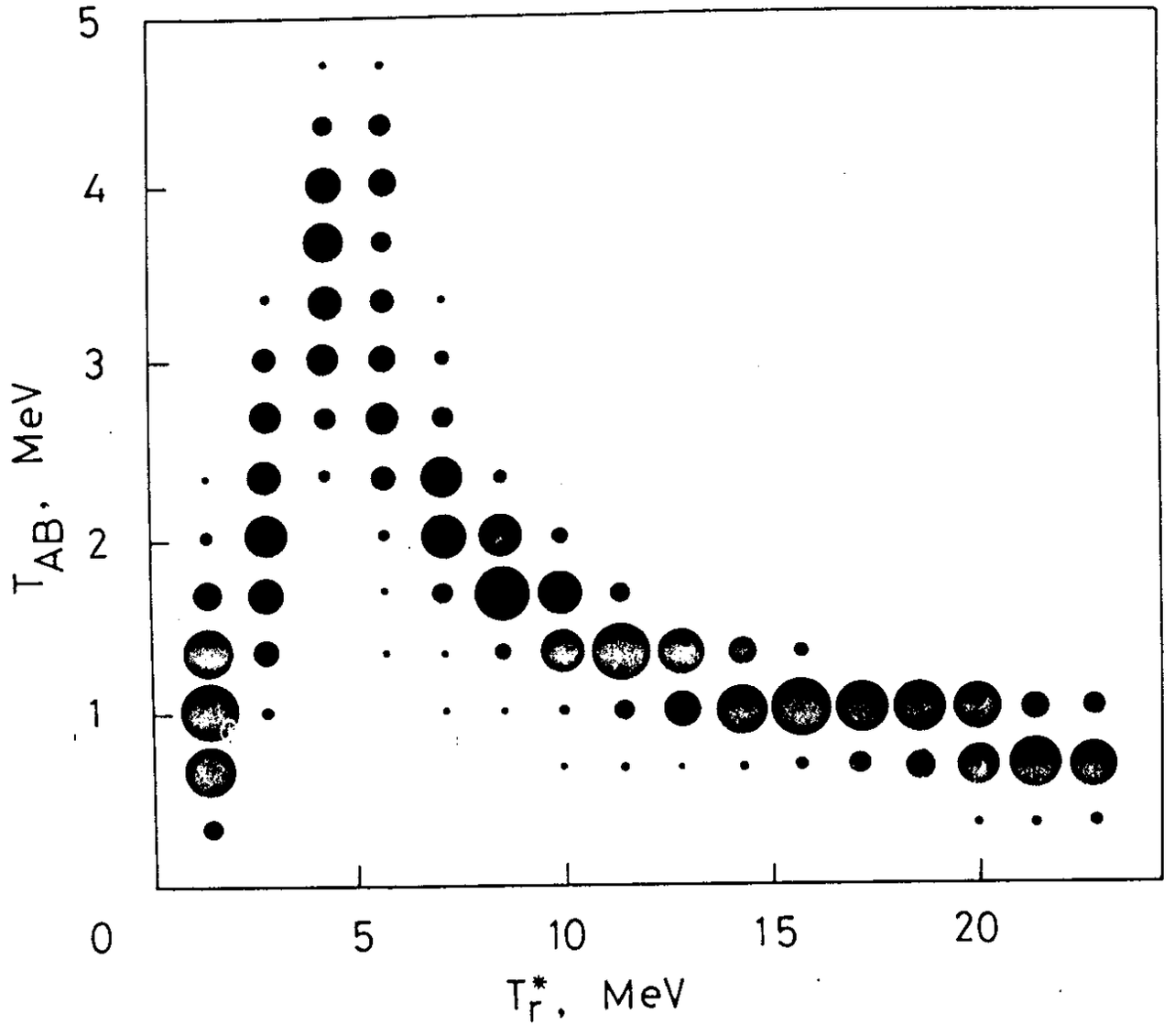

Fig. 7

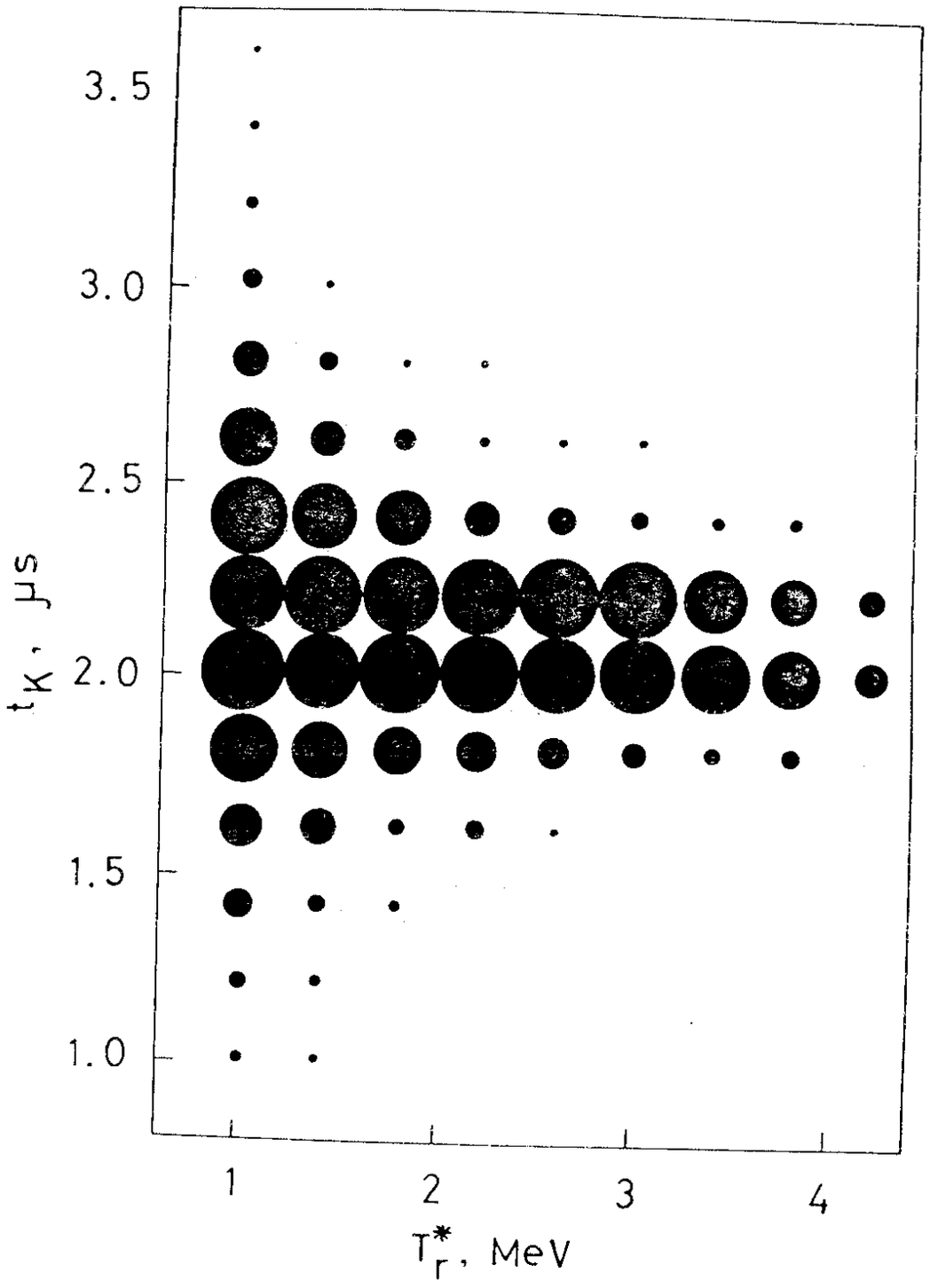

Fig. 8

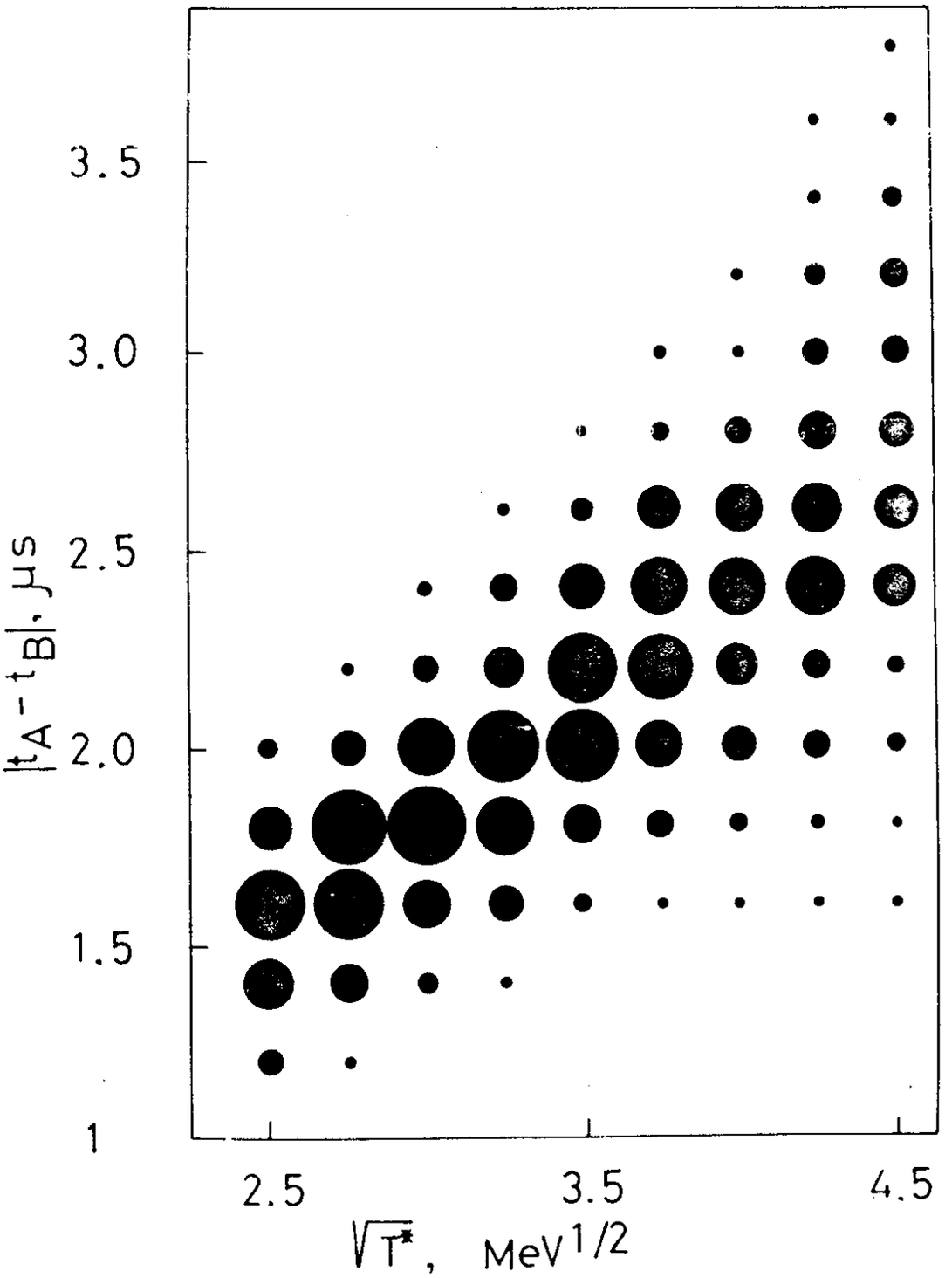

Fig. 9

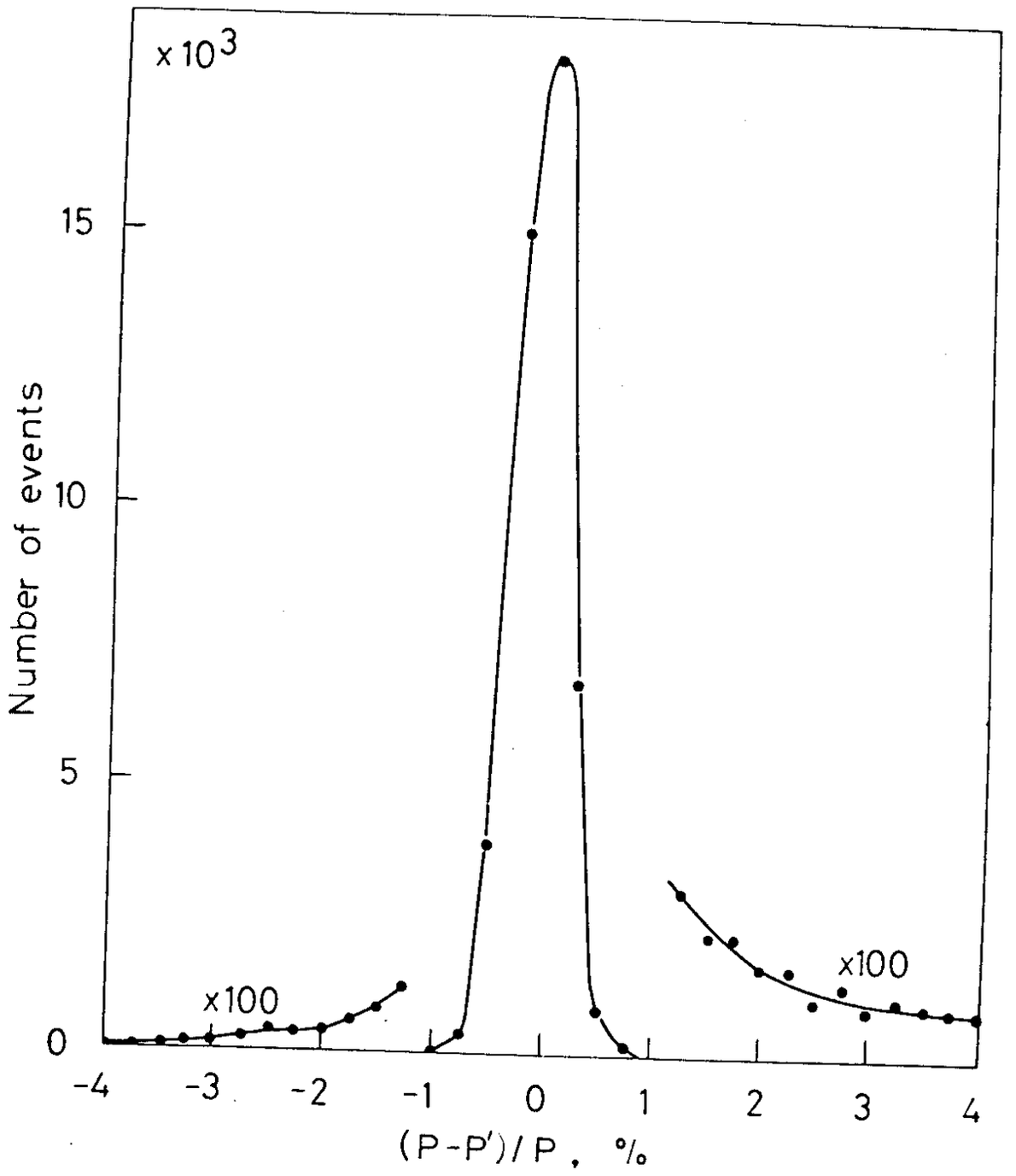

Fig. 10

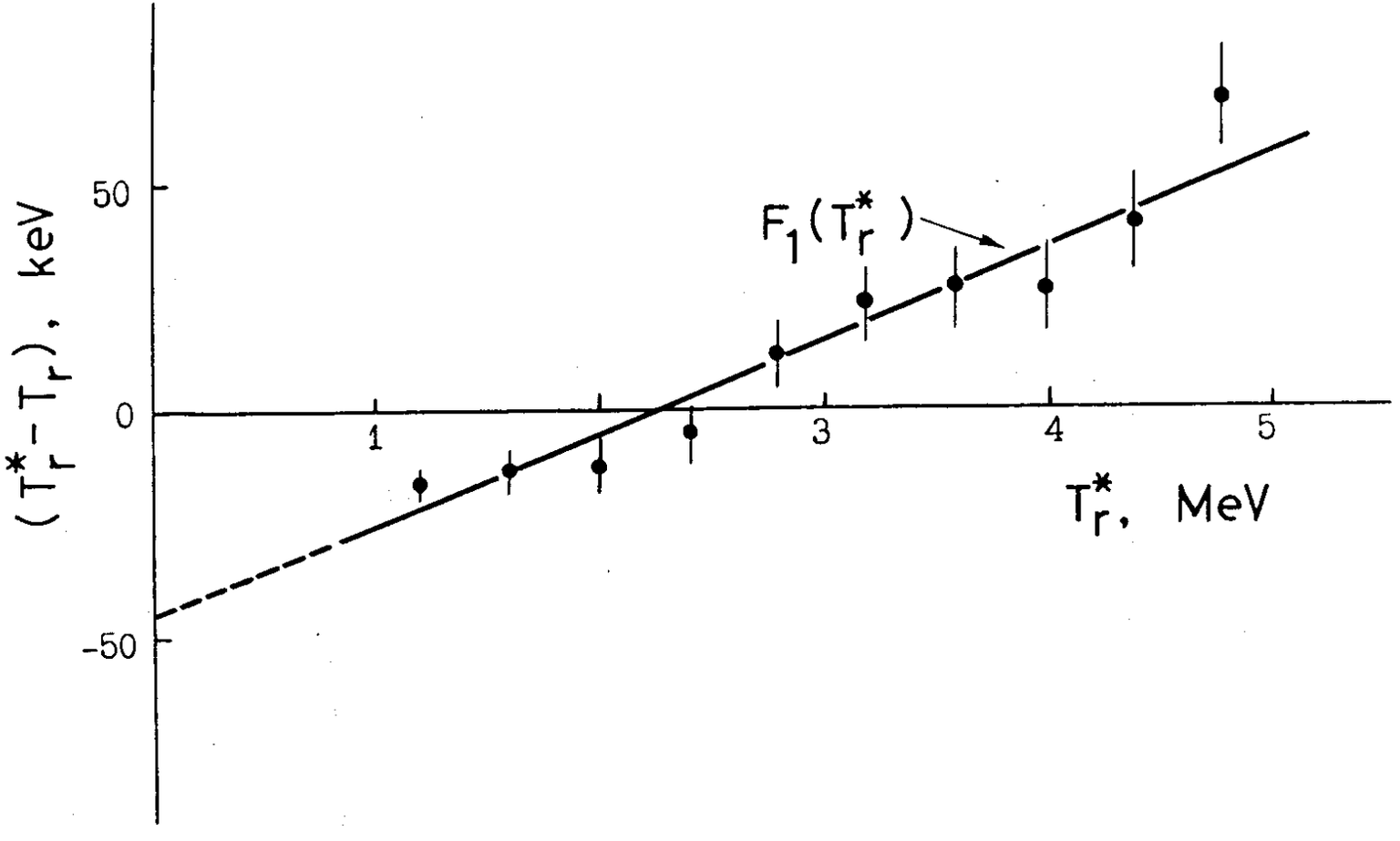

Fig. 11

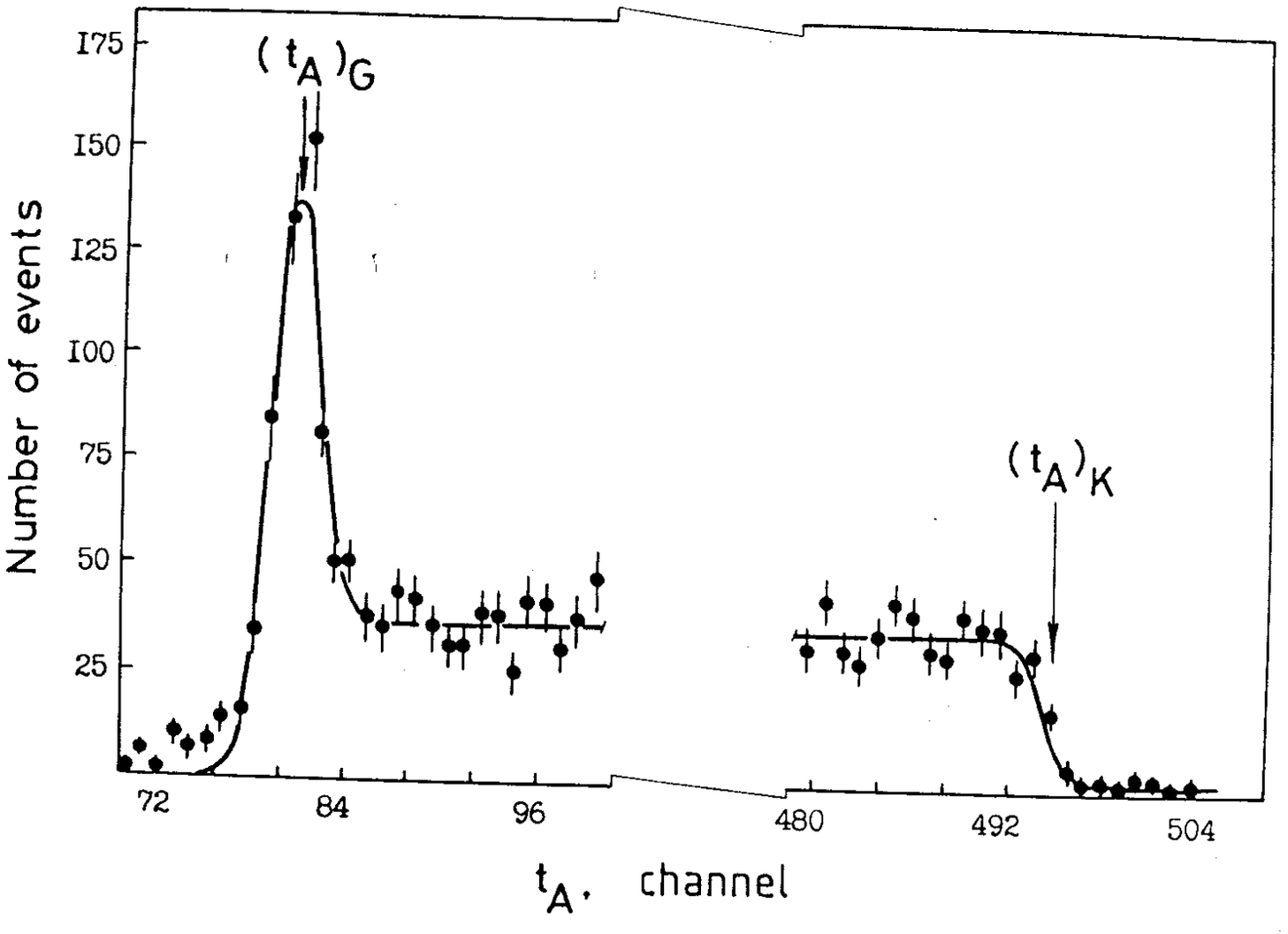
I75
I50
I25
I00
75
50
25
Number of events
$(t_A)_G$
$(t_A)_K$
72
84
96
480
492
504
t_A, channel

Fig. 12

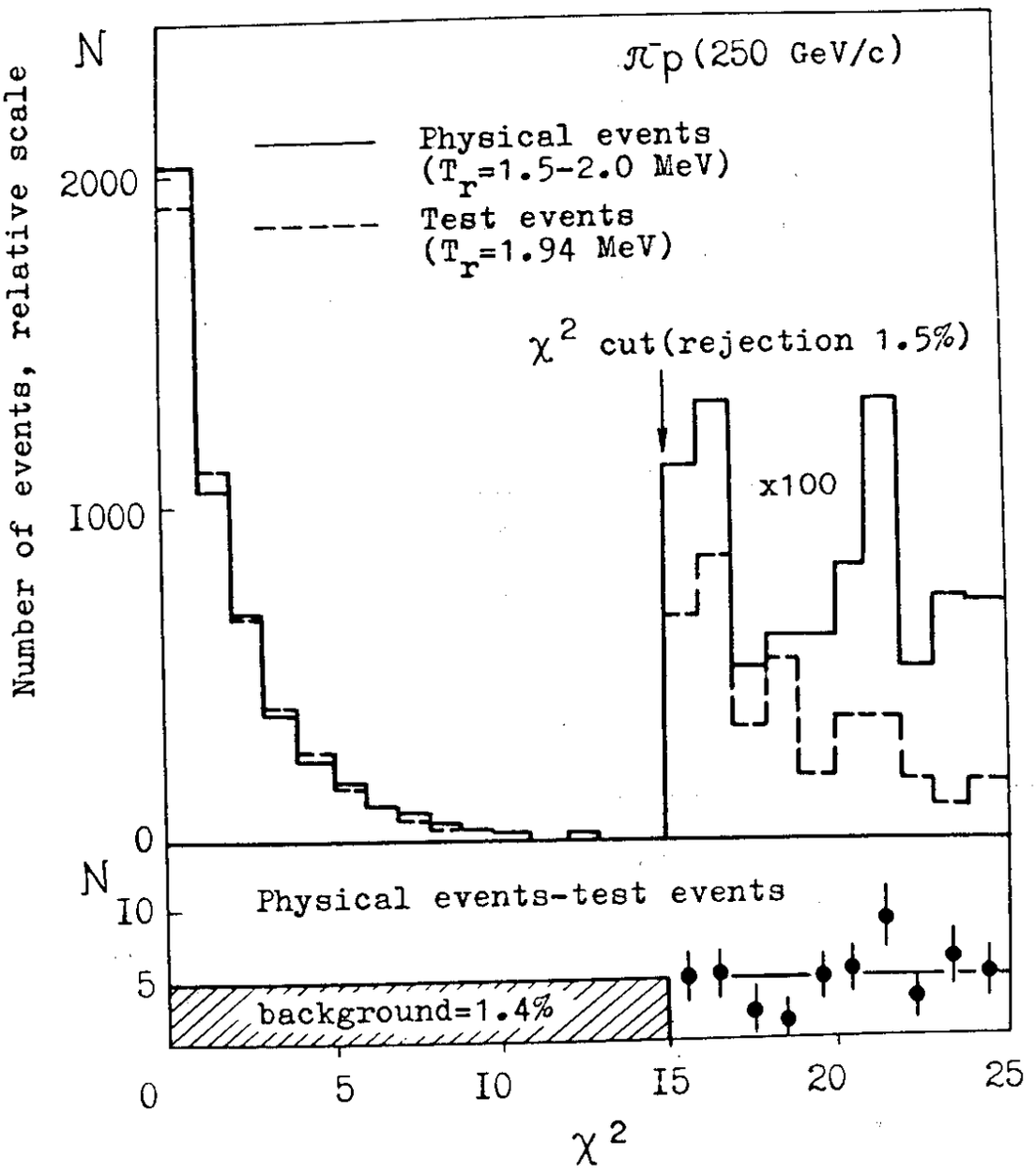
N
π^-p (250 GeV/c)
Physical events
(T_r=1.5-2.0 MeV)
Test events
(T_r=1.94 MeV)
χ^2 cut(rejection 1.5%)
x100
2000
1000
0
Number of events, relative scale
N
10
5
Physical events-test events
background=1.4%
0
5
10
15
20
25
χ^2

Fig. 13

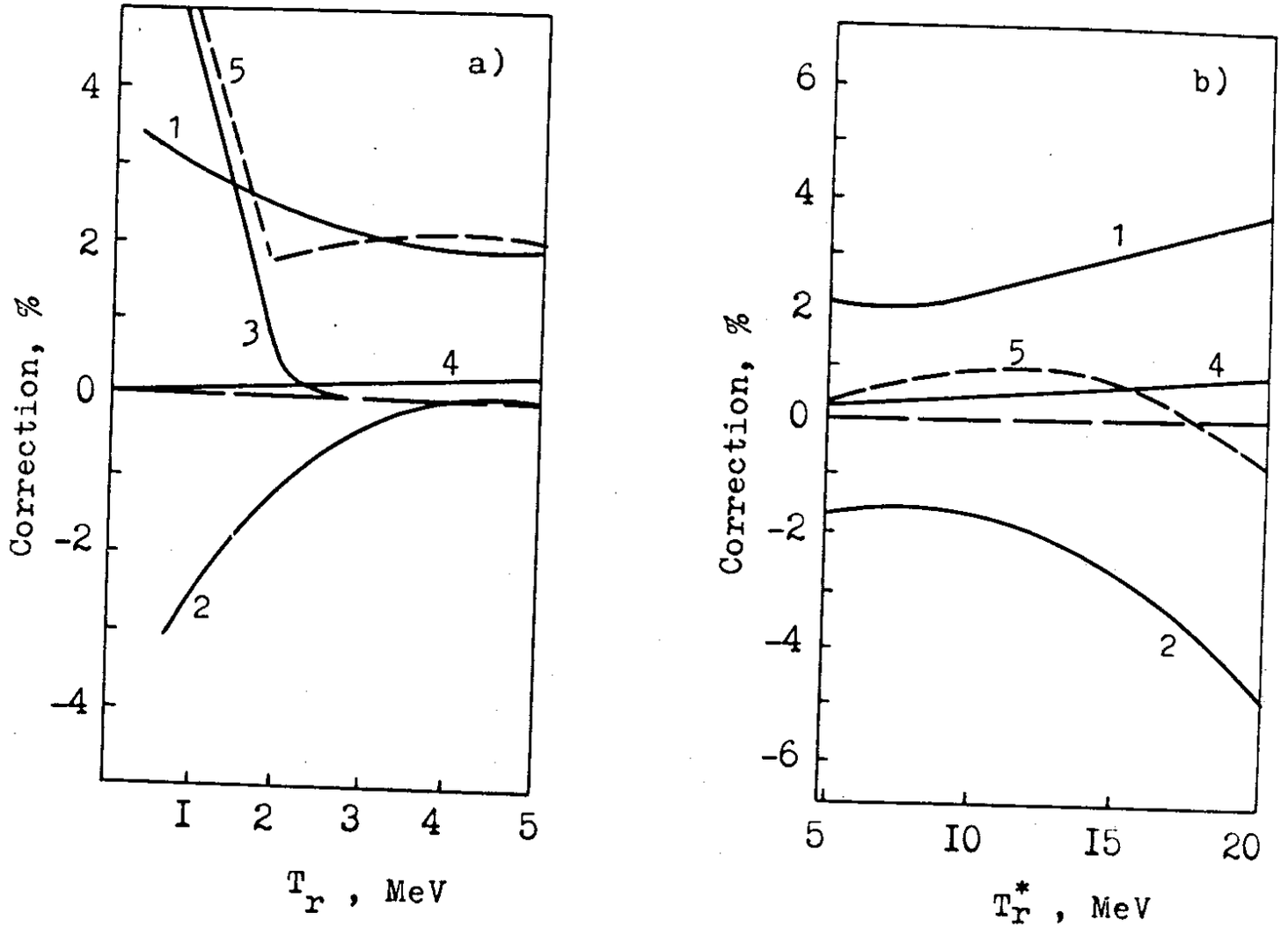

Fig. 14

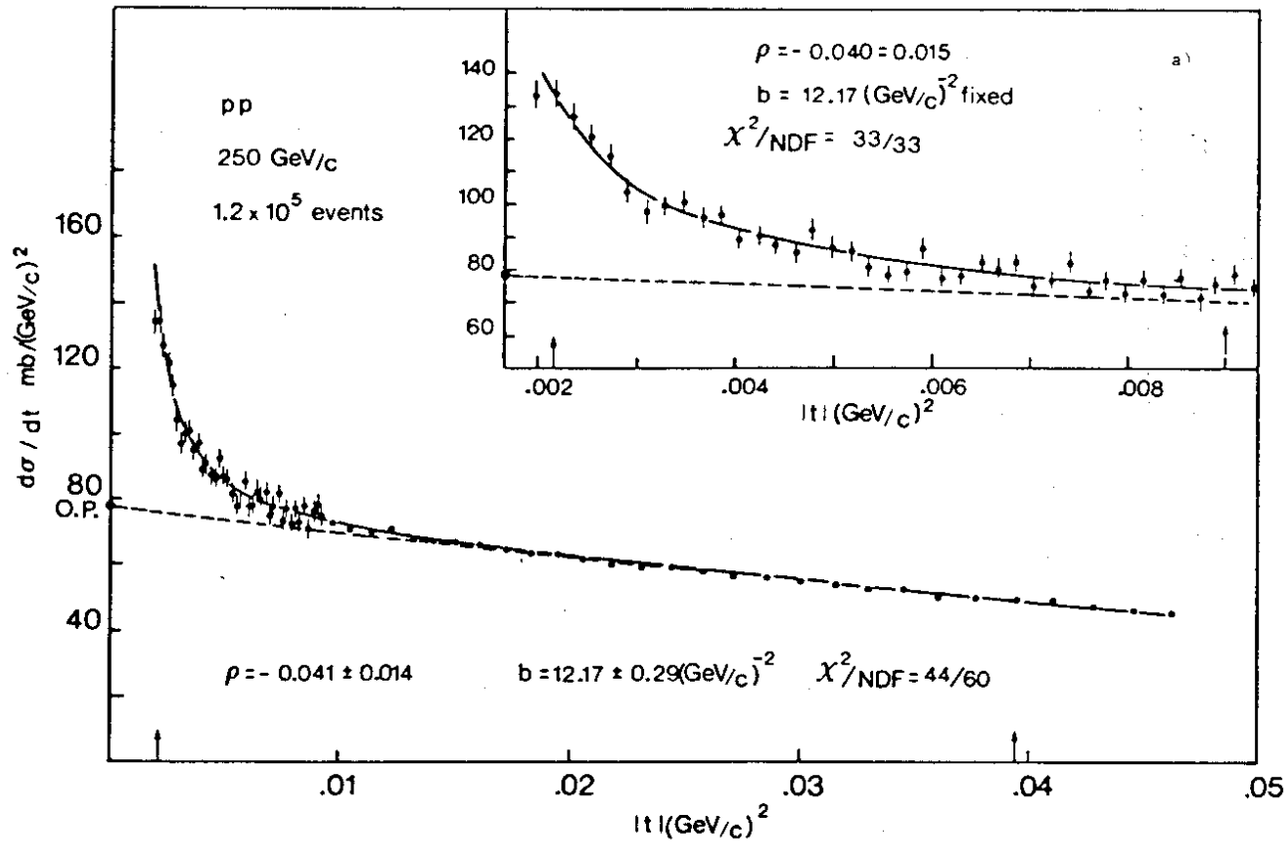
pp
250 GeV/c
1.2 x 10^5 events
ρ = - 0.040 ± 0.015
b = 12.17 (GeV/c)^-2 fixed
χ²/NDF = 33/33
a)
ρ = - 0.041 ± 0.014
b = 12.17 ± 0.29 (GeV/c)^-2
χ²/NDF = 44/60
O.P.
dσ / dt mb/(GeV/c)²
|t| (GeV/c)²

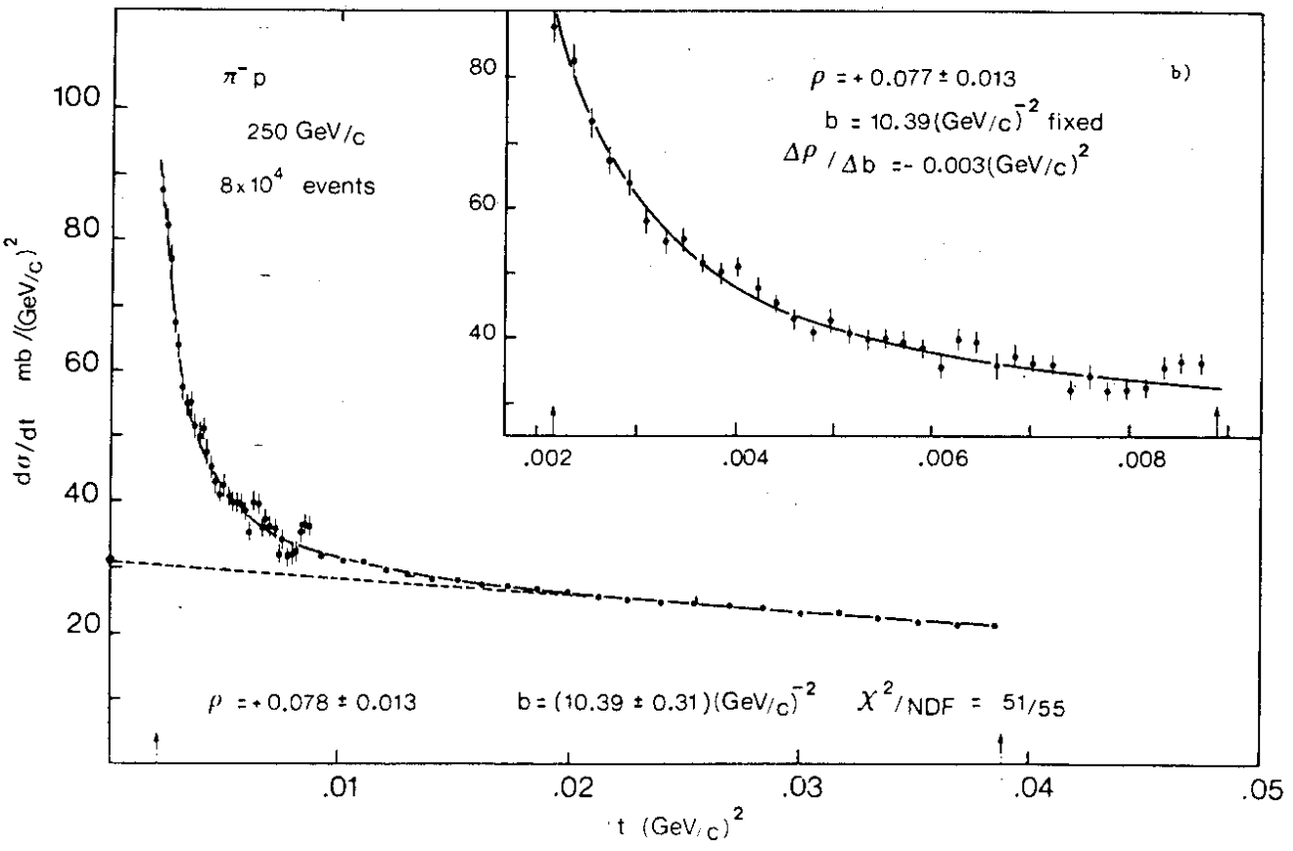
π⁻ p
250 GeV/c
8 x 10^4 events
ρ = + 0.077 ± 0.013
b = 10.39 (GeV/c)^-2 fixed
Δρ / Δb = - 0.003 (GeV/c)²
b)
ρ = + 0.078 ± 0.013
b = (10.39 ± 0.31) (GeV/c)^-2
χ²/NDF = 51/55
dσ/dt mb/(GeV/c)²
t (GeV/c)²

Fig. 15

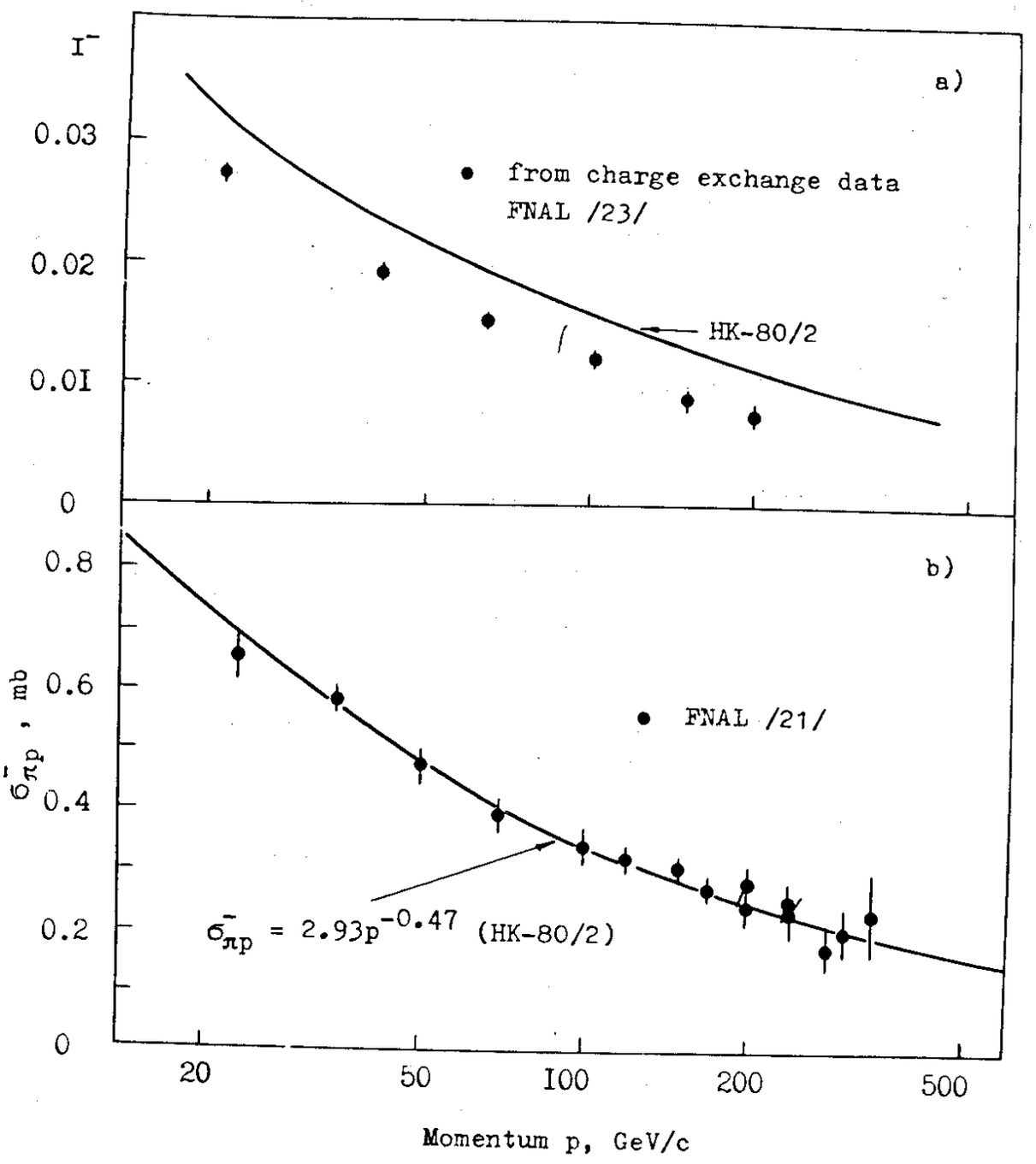
I⁻
a)
0.03
0.02
0.01
0
from charge exchange data
FNAL /23/
HK-80/2
b)
0.8
0.6
0.4
0.2
0
σ̄πp , mb
FNAL /21/
σ̄πp = 2.93p^-0.47 (HK-80/2)
20
50
100
200
500
Momentum p, GeV/c

Fig. 16

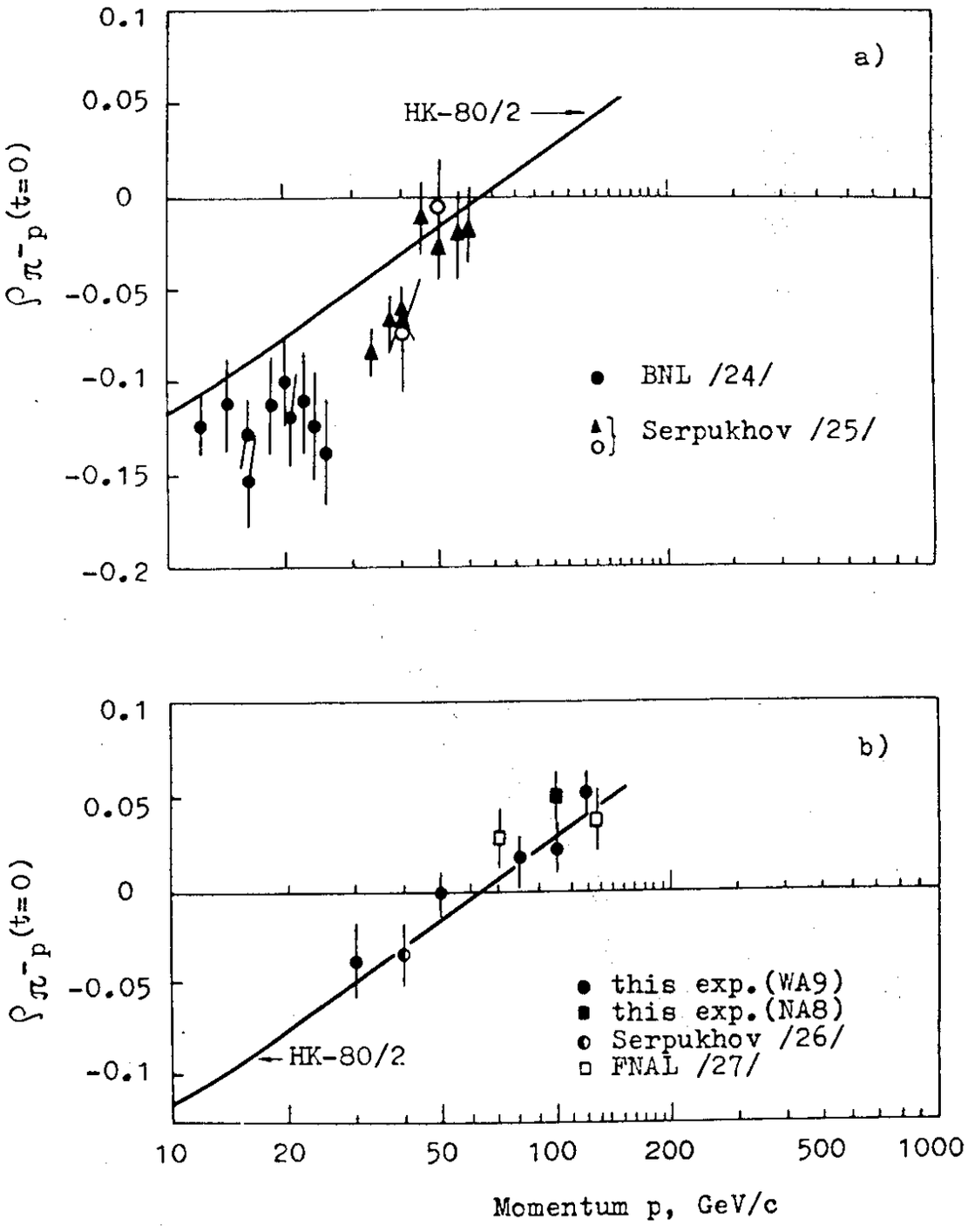
a)
HK-80/2
BNL /24/
Serpukhov /25/
b)
this exp.(WA9)
this exp.(NA8)
Serpukhov /26/
FNAL /27/
HK-80/2
$\rho_{\pi^- p}(t=0)$
Momentum p, GeV/c

Fig. 17

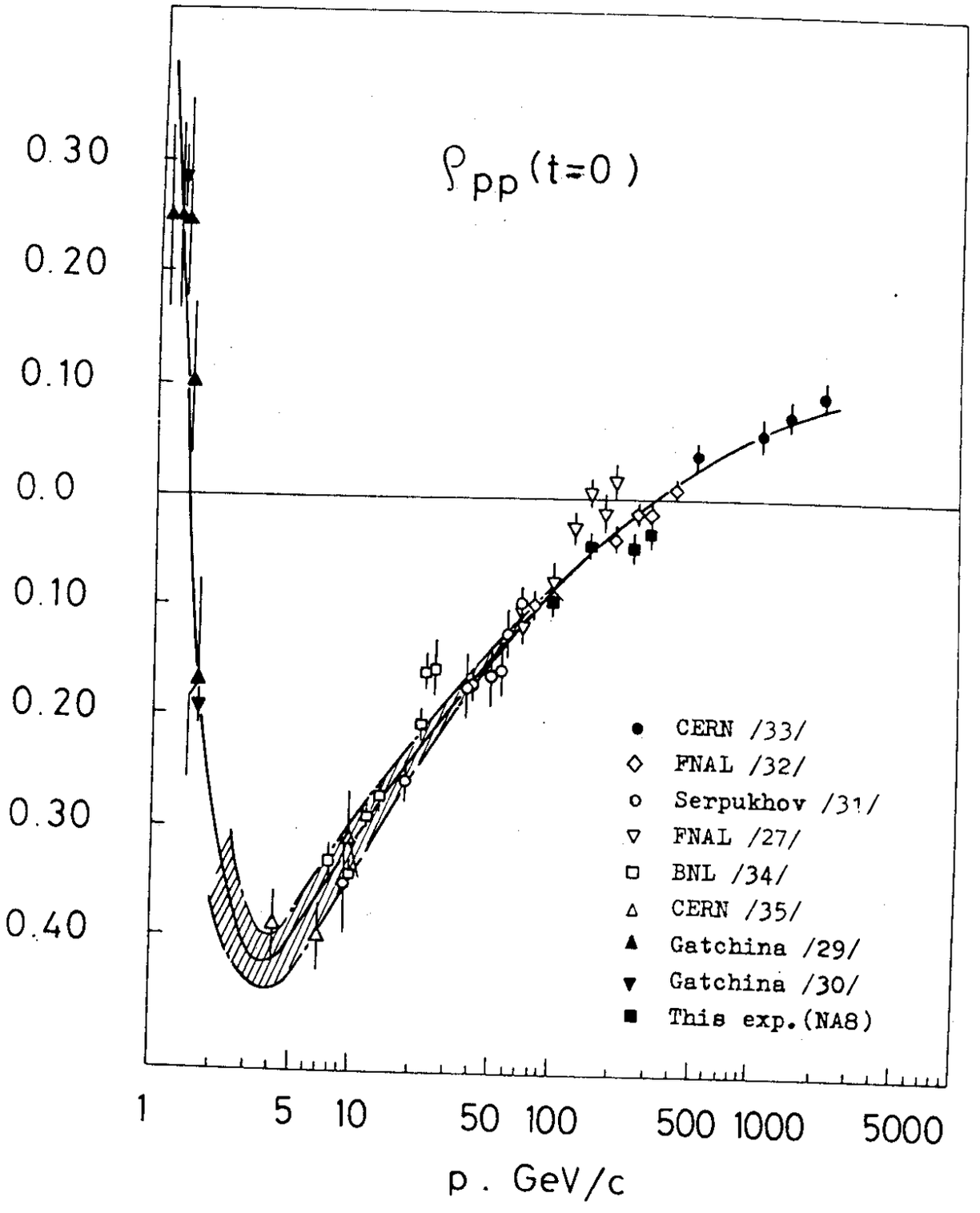
$\rho_{pp}(t=0)$
0.30
0.20
0.10
0.0
0.10
0.20
0.30
0.40
1
5
10
50
100
500
1000
5000
p . GeV/c
CERN /33/
FNAL /32/
Serpukhov /31/
FNAL /27/
BNL /34/
CERN /35/
Gatchina /29/
Gatchina /30/
This exp.(NA8)

Fig. 18

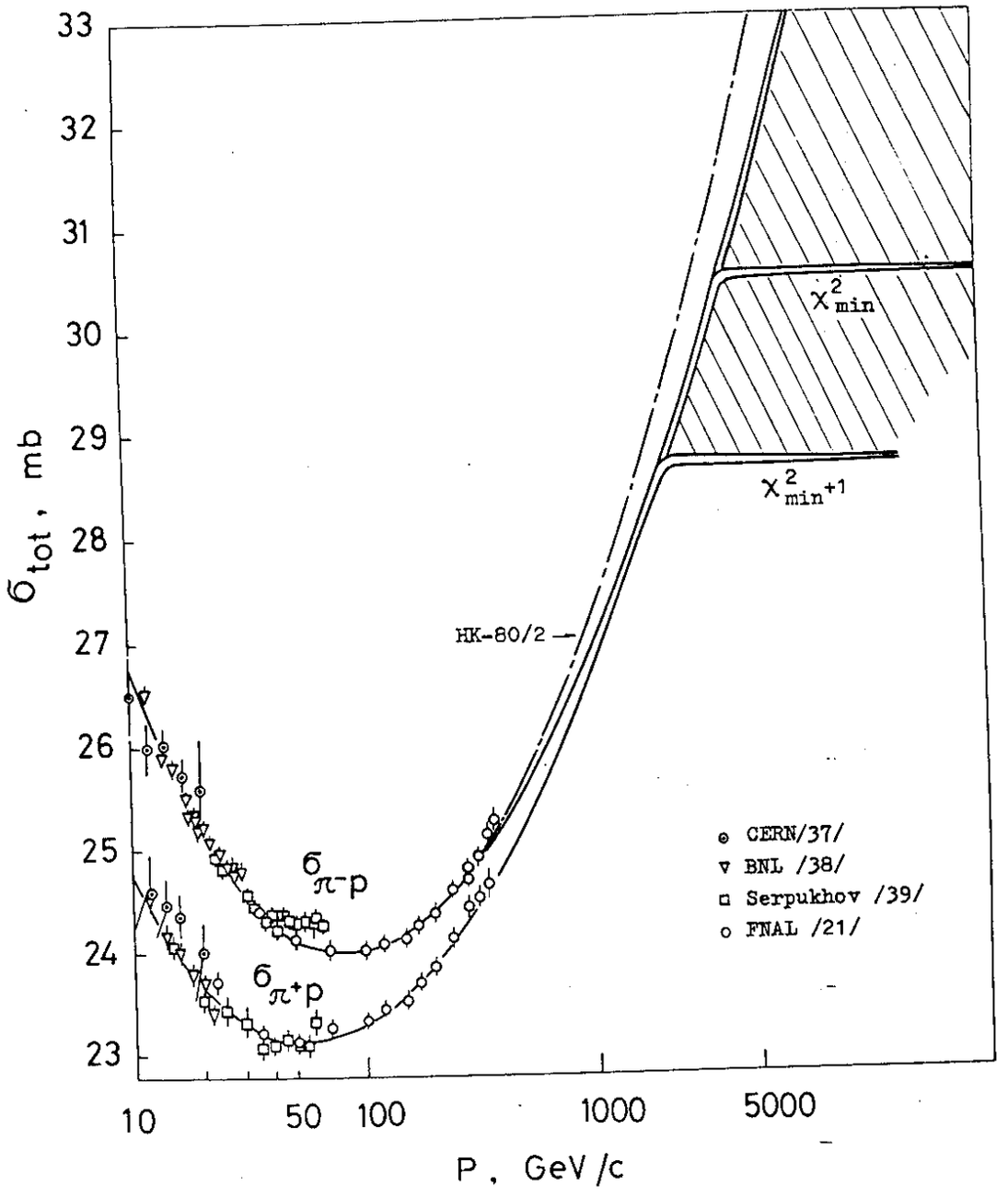
33
32
31
30
29
28
27
26
25
24
23
σ_{tot}, mb
10
50
100
1000
5000
P, GeV/c
σ_{π^-p}
σ_{π^+p}
χ^2_{min}
χ^2_{min+1}
НК-80/2
CERN/37/
BNL /38/
Serpukhov /39/
FNAL /21/

Fig. 19

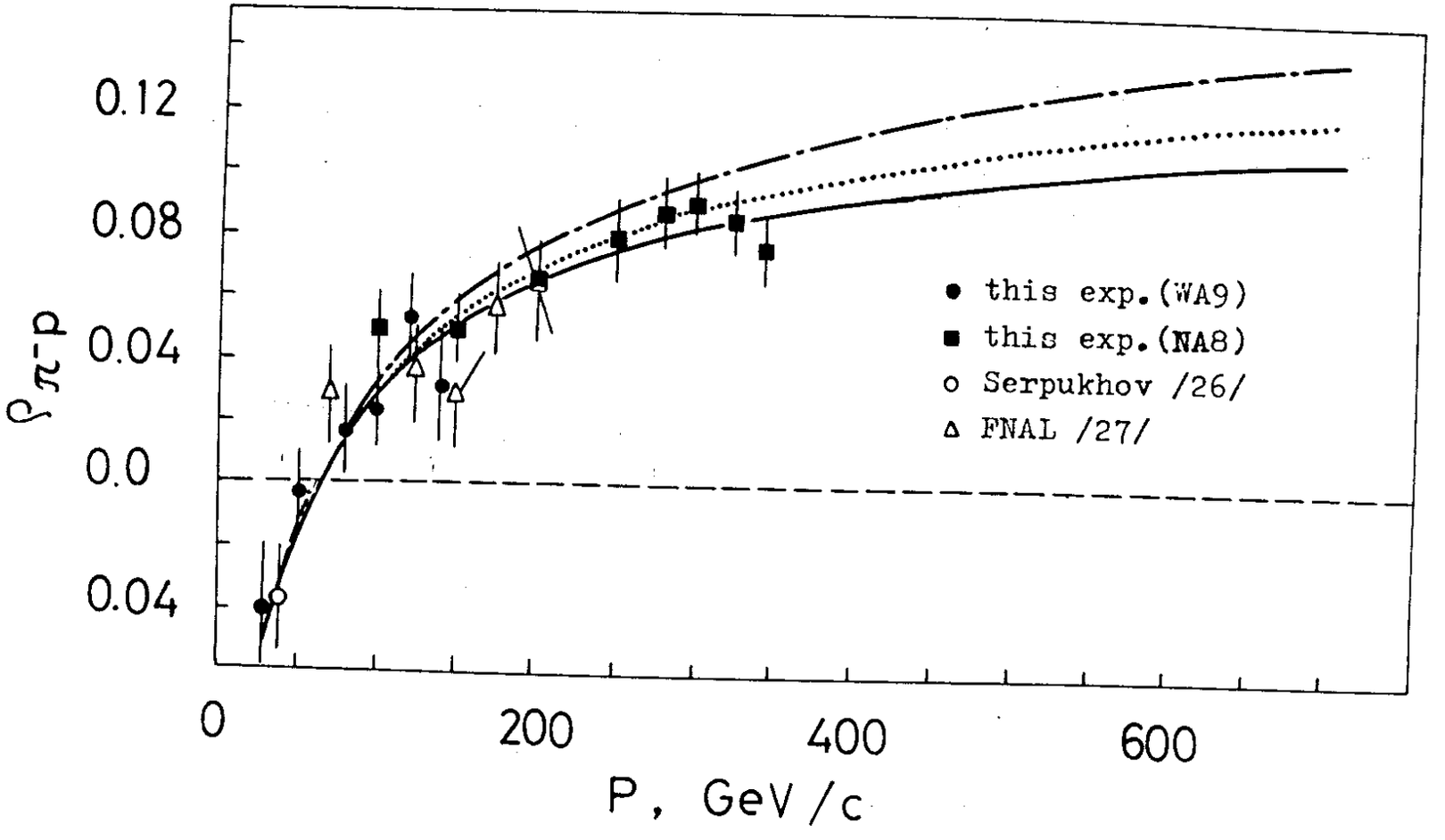
0.12
0.08
0.04
0.0
0.04
$\rho_{\pi^- p}$
0
200
400
600
P, GeV/c
this exp.(WA9)
this exp.(NA8)
Serpukhov /26/
FNAL /27/

Fig. 20

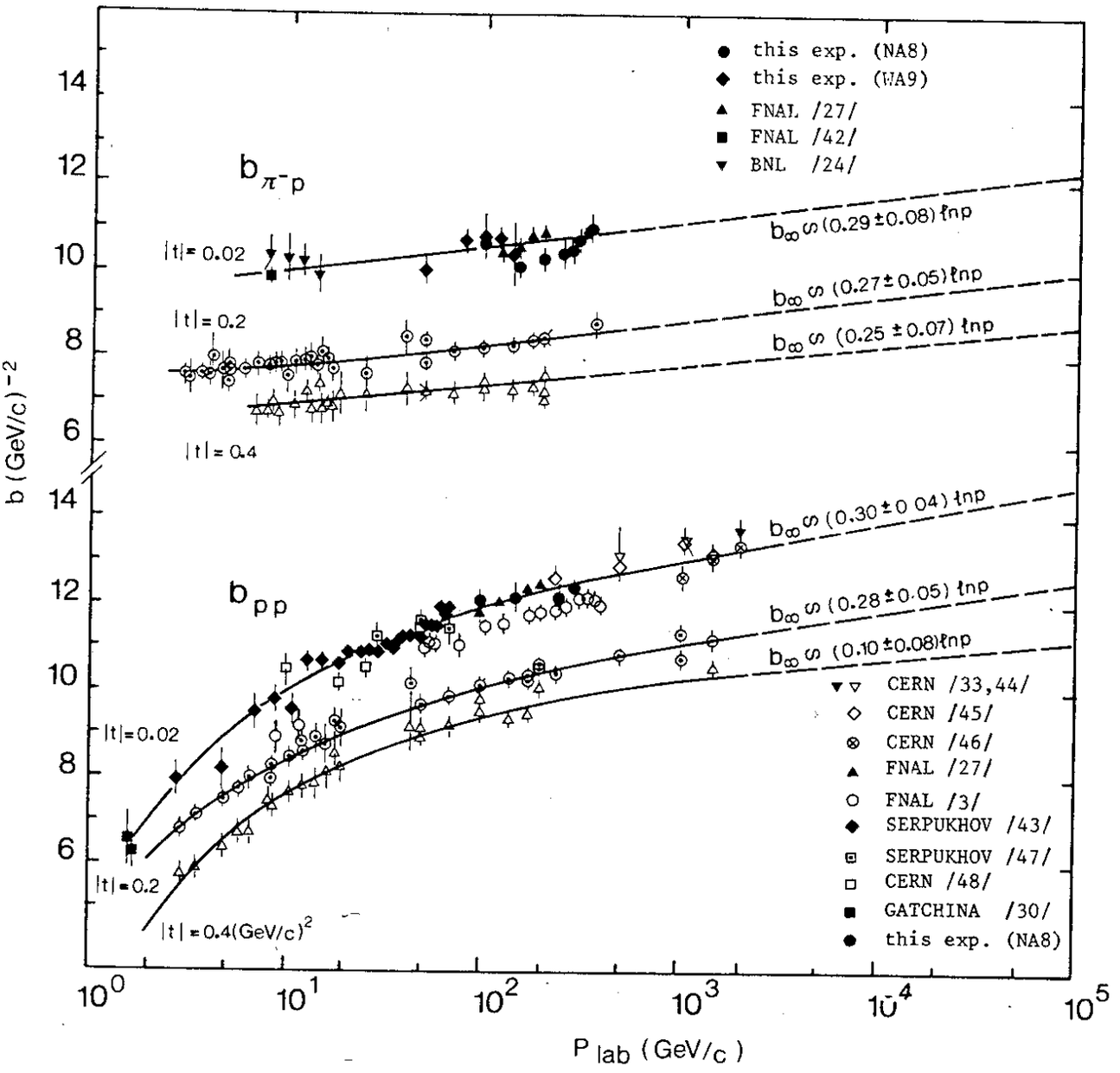
this exp. (NA8)
this exp. (WA9)
FNAL /27/
FNAL /42/
BNL /24/
$b_{\pi^- p}$
|t|= 0.02
|t| = 0.2
|t| = 0.4
$b_{\infty} s^{(0.29 \pm 0.08)} \ln p$
$b_{\infty} s^{(0.27 \pm 0.05)} \ln p$
$b_{\infty} s^{(0.25 \pm 0.07)} \ln p$
b_{pp}
$b_{\infty} s^{(0.30 \pm 0.04)} \ln p$
$b_{\infty} s^{(0.28 \pm 0.05)} \ln p$
$b_{\infty} s^{(0.10 \pm 0.08)} \ln p$
|t|=0.02
|t|=0.2
$|t| = 0.4 (GeV/c)^2$
CERN /33,44/
CERN /45/
CERN /46/
FNAL /27/
FNAL /3/
SERPUKHOV /43/
SERPUKHOV /47/
CERN /48/
GATCHINA /30/
this exp. (NA8)
b (GeV/c)$^{-2}$
P_{lab} (GeV/c)

Fig. 21

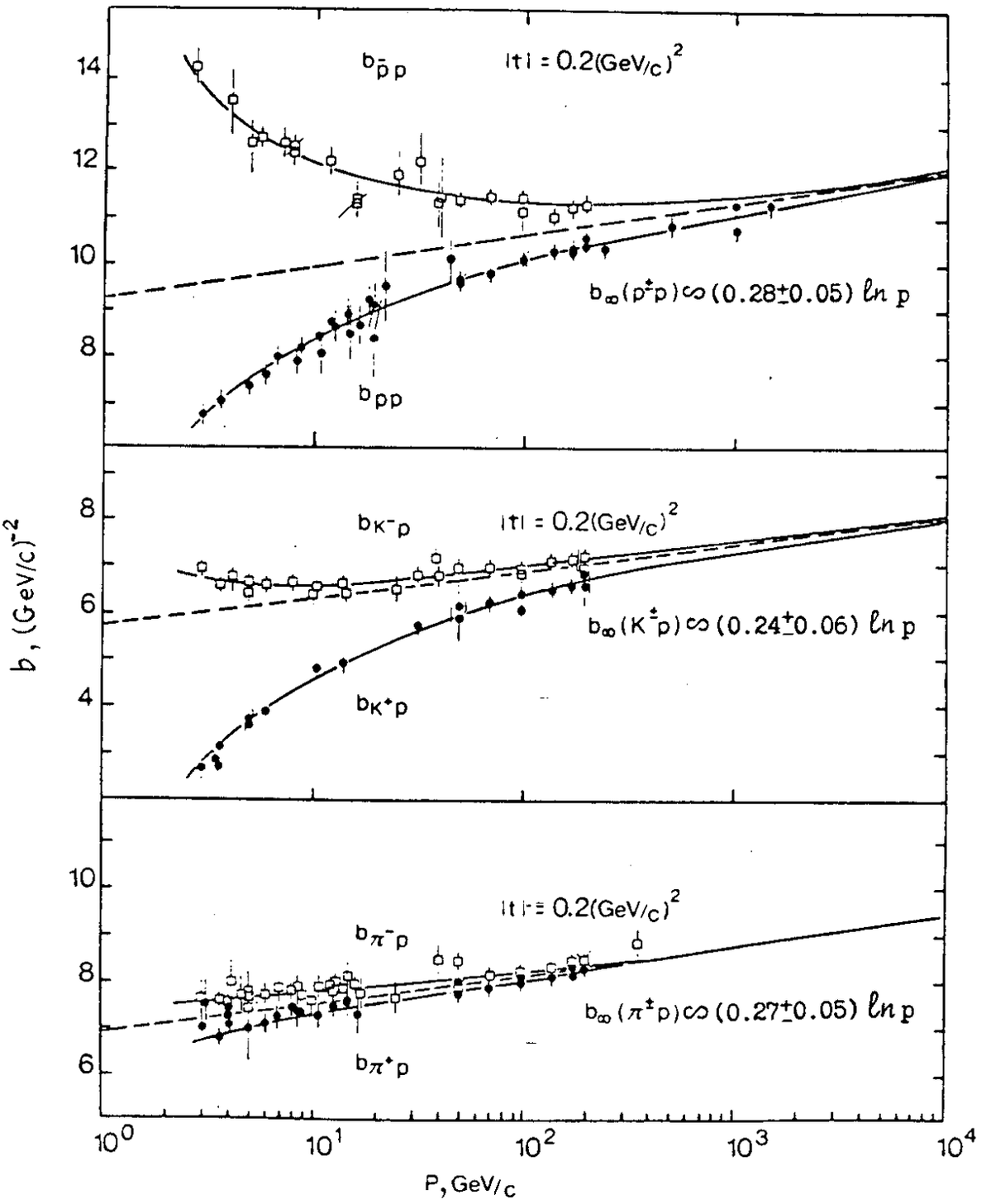
$b_{\bar{p}p}$
$|t| = 0.2(GeV/c)^2$
$b_{\infty}(p^{\pm}p) \propto (0.28 \pm 0.05) \ln p$
b_{pp}
b_{K^-p}
$|t| = 0.2(GeV/c)^2$
$b_{\infty}(K^{\pm}p) \propto (0.24 \pm 0.06) \ln p$
b_{K^+p}
$|t| = 0.2(GeV/c)^2$
b_{π^-p}
$b_{\infty}(\pi^{\pm}p) \propto (0.27 \pm 0.05) \ln p$
b_{π^+p}
$b, (GeV/c)^{-2}$
$P, GeV/c$

Fig. 22

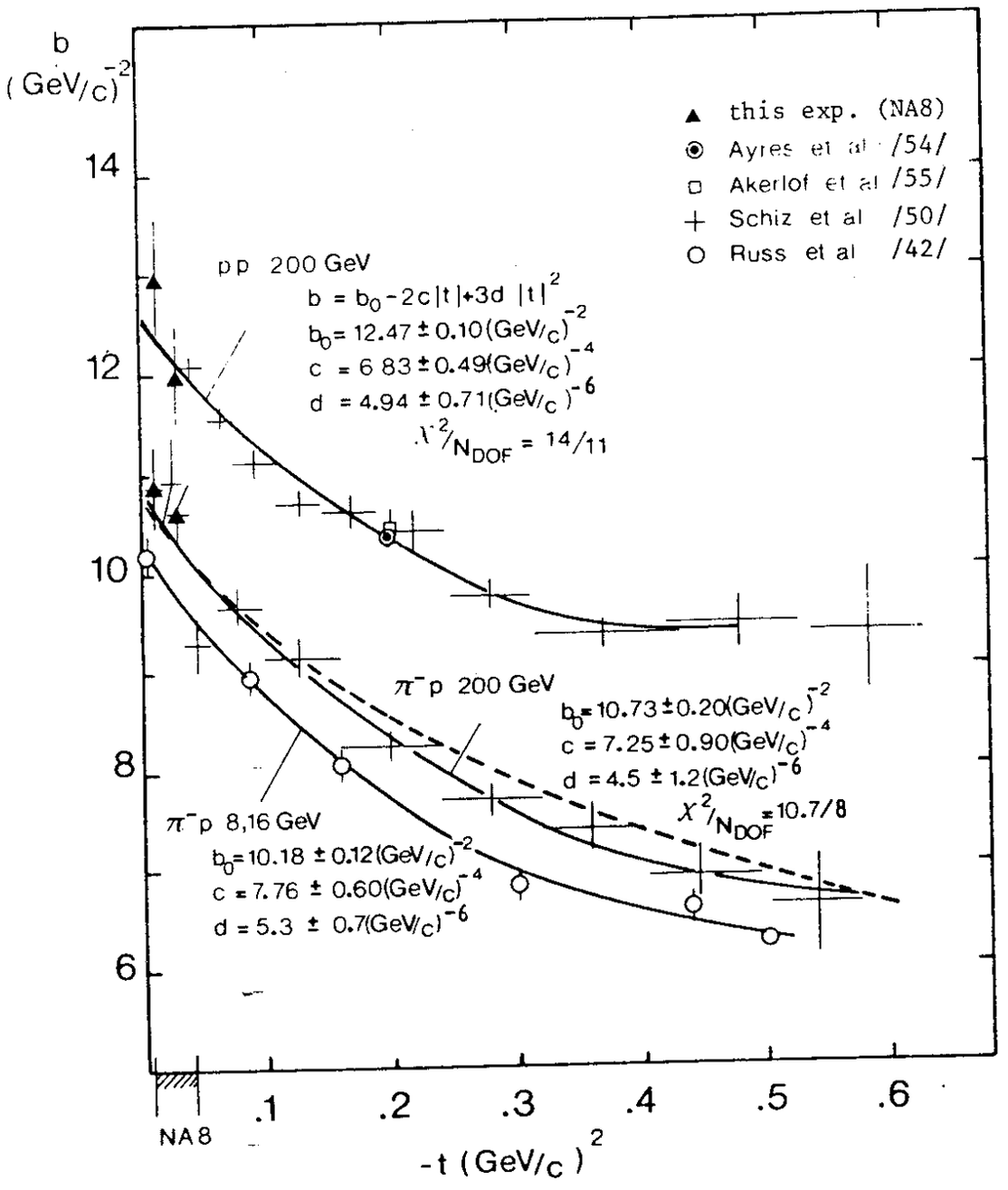
b
(GeV/c)$^{-2}$
14
12
10
8
6
▲ this exp. (NA8)
◉ Ayres et al /54/
□ Akerlof et al /55/
+ Schiz et al /50/
○ Russ et al /42/
pp 200 GeV
b = b$_0$ - 2c|t| + 3d |t|^2
b$_0$ = 12.47 ± 0.10 (GeV/c)$^{-2}$
c = 6.83 ± 0.49 (GeV/c)$^{-4}$
d = 4.94 ± 0.71 (GeV/c)$^{-6}$
χ^2/N_{DOF} = 14/11
π^-p 200 GeV
b$_0$ = 10.73 ± 0.20 (GeV/c)$^{-2}$
c = 7.25 ± 0.90 (GeV/c)$^{-4}$
d = 4.5 ± 1.2 (GeV/c)$^{-6}$
χ^2/N_{DOF} = 10.7/8
π^-p 8,16 GeV
b$_0$ = 10.18 ± 0.12 (GeV/c)$^{-2}$
c = 7.76 ± 0.60 (GeV/c)$^{-4}$
d = 5.3 ± 0.7 (GeV/c)$^{-6}$
NA8
.1
.2
.3
.4
.5
.6
-t (GeV/c)^2

Fig. 23